

Summer 2016

# Direct and inverse scattering problems for domains with multiple corners

Jiang Yihong

Follow this and additional works at: <https://digitalcommons.latech.edu/dissertations>

 Part of the [Computer Sciences Commons](#)

---

**DIRECT AND INVERSE SCATTERING PROBLEMS FOR  
DOMAINS WITH MULTIPLE CORNERS**

by

Yihong Jiang, B.S.

A Dissertation Presented in Partial Fulfillment  
of the Requirements of the Degree  
Doctor of Philosophy

COLLEGE OF ENGINEERING AND SCIENCE  
LOUISIANA TECH UNIVERSITY

August 2016

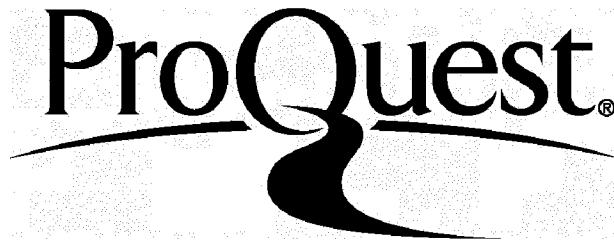
ProQuest Number: 10301527

All rights reserved

INFORMATION TO ALL USERS

The quality of this reproduction is dependent upon the quality of the copy submitted.

In the unlikely event that the author did not send a complete manuscript and there are missing pages, these will be noted. Also, if material had to be removed, a note will indicate the deletion.



ProQuest 10301527

Published by ProQuest LLC(2017). Copyright of the Dissertation is held by the Author.

All rights reserved.

This work is protected against unauthorized copying under Title 17, United States Code.  
Microform Edition © ProQuest LLC.

ProQuest LLC  
789 East Eisenhower Parkway  
P.O. Box 1346  
Ann Arbor, MI 48106-1346

LOUISIANA TECH UNIVERSITY

THE GRADUATE SCHOOL

MAY 20, 2016

Date

We hereby recommend that the dissertation prepared under our supervision by

Yihong Jiang, B.S.

Entitled

Direct And Inverse Scattering Problems For Domains With Multiple Corners

be accepted in partial fulfillment of the requirements for the Degree of

Ph.D. in Computational Analysis and Modeling

Hon Songyij

Supervisor of Dissertation Research

Weizhiyuan Du

Head of Department

Computational Analysis and Modeling

Department

Recommendation concurred in:

Weizhiyuan Du

Dan...

...

Jintao Kanro

Advisory Committee

Approved:

...

Director of Graduate Studies

Approved:

Sheel S. Shoman

Dean of the Graduate School

Hisham Hegab / SD

Dean of the College

## ABSTRACT

Direct and inverse scattering problems have wide applications in geographical exploration, radar, sonar, medical imaging and non-destructive testing. In many applications, the obstacles are not smooth. Corner singularity challenges the design of a forward solver. Also, the nonlinearity and ill-posedness of the inverse problem challenge the design of an efficient, robust and accurate imaging method.

This dissertation presents numerical methods for solving the direct and inverse scattering problems for domains with multiple corners. The acoustic wave is sent from the transducers, scattered by obstacles and received by the transducers. This forms the response matrix data. The goal for the direct scattering problem is to compute the response matrix data using the knowledge of the shape of the obstacles. The goal for the inverse scattering problem is to image the location and geometry of the obstacles based on the response matrix data. Both the near field and far field cases are considered. For the direct problem, the challenges of logarithmic singularity from Green's functions and corner singularity are both taken care of. For the inverse problem, an efficient and robust direct imaging method similar to the Multiple Signal Classification algorithm is proposed. Multiple frequency data are combined to capture details while not losing robustness. The near field and far field response matrices are compared and their singular value patterns are compared as well. The singular value perturbation is carefully studied. Extensive numerical results demonstrate that our forward solver is capable of handling domains with multiple corners by solving a linear system with low condition numbers

generated from a boundary integral equation, that our inverse problem solver is efficient, accurate and robust. It could handle response matrix data with noise.

## APPROVAL FOR SCHOLARLY DISSEMINATION

The author grants to the Prescott Memorial Library of Louisiana Tech University the right to reproduce, by appropriate methods, upon request, any or all portions of this dissertation. It is understood that "proper request" consists of the agreement, on the part of the requesting party, that said reproduction is for his personal use and that subsequent reproduction will not occur without written approval of the author of this dissertation. Further, any portions of the dissertation used in books, papers, and other works must be appropriately referenced to this dissertation.

Finally, the author of this dissertation reserves the right to publish freely, in the literature, at any time, any or all portions of this dissertation.

Author Yihong Jiang

Date 07/14/2016

## **DEDICATION**

This dissertation is dedicated to my parents for their love and support.

## TABLE OF CONTENTS

ABSTRACT .....	iii
DEDICATION.....	vi
LIST OF TABLES.....	viii
LIST OF FIGURES .....	ix
ACKNOWLEDGMENTS .....	xi
CHAPTER 1 INTRODUCTION.....	1
CHAPTER 2 BACKGROUND.....	4
2.1    The Direct Scattering Problem .....	4
2.2    The Inverse Scattering Problem .....	14
CHAPTER 3 METHODS.....	22
3.1    The Forward Problem.....	22
3.2    The Inverse Problem.....	29
CHAPTER 4 RESULTS.....	41
4.1    The Forward Problem.....	41
4.2    The Inverse Problem.....	49
CHAPTER 5 CONCLUSIONS AND FUTURE WORK.....	64
5.1    Conclusions .....	64
5.2    Future Work.....	64
BIBLIOGRAPHY.....	66

## LIST OF TABLES

<b>Table 4-1:</b> Error of “Kite” with Grid Number $n = 16, 32, 64$ . .....	42
<b>Table 4-2:</b> Response Matrix Error ( $n = 16$ ) ( $\times 10^{-3}$ ). .....	43
<b>Table 4-3:</b> Response Matrix Error ( $n = 32$ ) ( $\times 10^{-4}$ ). .....	44
<b>Table 4-4:</b> Response Matrix Error ( $n = 64$ ) ( $\times 10^{-6}$ ). .....	44
<b>Table 4-5:</b> Error of “Corners” with Grid Number ( $n = 16, 32, 64$ ). .....	45
<b>Table 4-6:</b> Response Matrix Error ( $k = 7, n = 16$ ). .....	46
<b>Table 4-7:</b> Response Matrix Error ( $k = 7, n = 32$ ) ( $\times 10^{-4}$ ). .....	46
<b>Table 4-8:</b> Error of “Butterfly” with $n = 16, 32$ . .....	46
<b>Table 4-9:</b> Response Matrix Error ( $k = 4, n = 16$ ) .....	59
<b>Table 4-10:</b> Response Matrix Error ( $k = 4, n = 32$ ) ( $\times 10^{-5}$ ) .....	59
<b>Table 4-11:</b> Response Matrix Error ( $k = 7, n = 16$ ) .....	60
<b>Table 4-12:</b> Response Matrix Error ( $k = 7, n = 32$ ) .....	60

## LIST OF FIGURES

<b>Figure 3-1:</b> Setup for Inverse Problems.....	30
<b>Figure 3-2:</b> Imaging Results ( $M = 1, 5, 18, 24$ for Row 1 and $M = 30, 36, 42, 48$ for Row 2). [25].....	35
<b>Figure 3-3:</b> Singular Value Perturbation for 10,000 Realizations.....	40
<b>Figure 3-4:</b> Singular Value Count Falling into Consecutive Intervals with Equal Spacing. ....	40
<b>Figure 4-1:</b> The Mesh for “Kite” Shape. ....	42
<b>Figure 4-2:</b> “Three Corners” with Graded Mesh.....	44
<b>Figure 4-3:</b> “Butterfly” with Graded Mesh.....	47
<b>Figure 4-4:</b> Singular Value Plots for Near and Far Field Response Matrices. ....	48
<b>Figure 4-5:</b> “Butterfly” with Plane Incident Wave, Far Field Data.....	50
<b>Figure 4-6:</b> “Butterfly” Plane Incident Wave, near Field Data with $r = 5$ .....	51
<b>Figure 4-7:</b> “Butterfly” Point Source with $r = 5$ , Far Field Data. ....	52
<b>Figure 4-8:</b> “Butterfly” Point Source with $r = 5$ , near Field Data with $r = 5$ . ....	53
<b>Figure 4-9:</b> “Butterfly” with Plane Incident Wave, Far Field Data with Noise. ....	54
<b>Figure 4-10:</b> “Butterfly” Plane Incident Wave, near Field Data with $r = 5$ with Noise...55	
<b>Figure 4-11:</b> “Butterfly” Point Source with $r = 5$ , Far Field Data with Noise.....	56
<b>Figure 4-12:</b> “Butterfly” Point Source with $r = 5$ , near Field Data with $r = 5$ with Noise.....	57
<b>Figure 4-13:</b> “Paw” with Graded Mesh. ....	58
<b>Figure 4-14:</b> “Paw” with Plane Incident Wave, Far Field Data. ....	61
<b>Figure 4-15:</b> Low Frequency Result for Multiple Targets. ....	62

**Figure 4-16: High Frequency Result for Multiple Targets.....62**  
**Figure 4-17: Zooming the Butterfly Shape Part using High Frequency.....63**

## **ACKNOWLEDGMENTS**

I would like to thank my advisors, Dr. Songming Hou and Dr. Weizhong Dai, for their guidance during my Ph.D. study. During the past five years, Dr. Hou spent an extensive amount of time tutoring me. Direct and inverse scattering problems is a research field not introduced in graduate textbooks. Dr. Hou helped me to prepare for the necessary background materials for the research and gave me quite some encouragement when I struggled with the research. Dr. Hou and Dr. Dai helped me to get accustomed to the U.S. culture as well.

I would also like to thank my committee members, Dr. Dave Meng, Dr. Jinko Kanno and Dr. Sumeet Dua, for their valuable inputs for my dissertation.

# CHAPTER 1

## INTRODUCTION

Scattering theory is a significant part of mathematical physics in the twentieth century. Scientists and mathematicians are attracted by these scattering phenomena. Basically, scattering theory is about analyzing the effect an inhomogeneous medium has on an incident particle or wave. The incoming acoustic or electromagnetic wave can be scattered by the target and transducers can receive it. The classical scattering problem can be separated into two parts: direct scattering problem and inverse scattering problem.

In direct scattering problem, the total field is viewed as the sum of an incident field  $u^i$  and a scattered field  $u^s$ . The goal is to determine  $u^s$  from the knowledge of  $u^i$  and the differential equation governing the wave motion.

In inverse scattering problem, the refractive index  $n(x)$  or the geometry of the target is unknown. Using the information of incident waves and the scattered waves recorded by the transducers to find out the target's location and geometry is the main objective of the inverse scattering problem.

For the forward problem, the smooth target case is studied by [1] using Nystrom discretization and boundary integral method. Exponential convergence is exhibited. A target with one corner is also studied by [1]. A change of variable technique is used to generate graded mesh to resolve the corner. High order convergence is observed.

Berenger [39] used a different approach, the perfectly matched layer technique, to truncate the unbounded domain to be a bounded domain. The finite difference method is used, and across the perfectly matched layer (PML), the solution has exponential decay and no reflection.

For the inverse problem, in [25], a direct imaging algorithm, the Multiple Signal Classification (MUSIC) algorithm is introduced for extended targets with near field data. In [26], the far field data is considered. In [27], multi-tone imaging method is introduced. Unlike the projection type MUSIC method, this method keeps phase information and combine multiple frequency data. In [29], an iterative continuation method is introduced by utilizing the MUSIC algorithm as an initial guess. It is an optimization method that minimizes the residual by solving many forward and adjoint problems. In [28], the linear sampling method is used to solve the inverse scattering problems. It uses a factorization of the far field operator. The method is closely related to the MUSIC algorithm.

In this dissertation research, for the forward problem, we study the more challenging problem with domains having multiple corners. The problem, though having wide applications, is not well-studied in the literature. If we strictly follow the idea from the previous work in [1] for a domain with one corner, the linear system would have a large condition number. The goal is to develop a well-conditioned forward solver. For the inverse problem, the MUSIC algorithm in [25] is a projection algorithm that does not keep the phase information. It is not meaningful to combine multiple frequency data directly. The goal is to use an efficient, robust and accurate direct imaging algorithm similar to the MUSIC algorithm while keeping the phase information to image a target containing multiple targets with corners.

The organization of the dissertation is as follows. In Chapter 2, the background of direct and inverse scattering problems are discussed. In Chapter 3, the method for the dissertation research is introduced. In Chapter 4, numerical results are presented. In Chapter 5, a summary and future work is presented.

## CHAPTER 2

### BACKGROUND

We present the background of our research in this chapter. Our research is divided into two parts: direct scattering problem and inverse scattering problem. For direct scattering problem, we describe the methodology in [1] for the domains with a smooth boundary in Section 2.1. Our research is for domains with multiple corners. For inverse scattering problem, we describe several approaches for imaging methods in Section 2.2. Our imaging method is similar to the MUSIC algorithm [25, 26] or the multi-tone imaging algorithm [27].

#### 2.1 The Direct Scattering Problem

Let  $u$  be the total field,  $u^i$  be the incident field, and  $u^s$  be the scattered field. Here,  $u^i$  comes from one position or one direction. The total field  $u$  can be written as **Eq. 2-1**:

$$u = u^i + u^s. \tag{Eq. 2-1}$$

Determining the scattered field  $u^s$  from the knowledge of the  $u^i$ , the shape of the target, and the differential equation governing the wave motion is called the direct scattering problem. There are two basic direct scattering problems: the scattering of time-harmonic acoustic or electromagnetic waves by a penetrable inhomogeneous medium of

compact support and by a bounded impenetrable obstacle. The impenetrable problem also has two different cases: sound soft case and sound hard case.

The total field should satisfy the Helmholtz equation:

$$\Delta u + k^2 u = 0, \quad \text{Eq. 2-2}$$

where the wave number  $k$  is given by the positive constant  $k = \omega/c$ ,  $c$  is the speed of sound and  $\omega$  is the frequency.

There are two different kinds of impenetrable objects. For a sound-soft target, the pressure of the total wave vanishes on the boundary. When we consider the scattering of a given incoming wave  $u^i$  by a sound-soft target  $D$ , the total wave  $u$  must satisfy the wave equation in the exterior  $\mathbb{R}^2 \setminus \partial D$  of  $D$  and a Dirichlet boundary condition  $u = 0$  on  $\partial D$ . In the same way, the scattering from sound-hard target leads to a Neumann boundary condition  $\frac{\partial u}{\partial \nu} = 0$  on  $\partial D$  since here the normal velocity of the acoustic wave vanishes on the boundary. So in general, an impedance boundary condition for the Helmholtz equation with a positive constant  $\lambda$  can be written as:

$$\frac{\partial u}{\partial \nu} + i\lambda u = 0, \quad \text{on } \partial D. \quad \text{Eq. 2-3}$$

For a penetrable obstacle  $D$  with constant density  $\rho_D$  and speed of sound  $C_D$ , the density and speed of sound are different from the same properties of the surrounding medium  $\mathbb{R}^2 \setminus \partial D$ . This change will lead to a transmission problem. The total field  $u = u^i + u^s$  should satisfy the Helmholtz equation with wave number  $k = \omega/c$ , where  $u^i$  is the incoming wave and the scattered wave is  $u^s$  in the surrounding medium. In addition, a transmitted wave in  $D$  need satisfy the Helmholtz equation with the wave number

$k_D = \omega/c_D$ . It should be noticed that  $k_D \neq k$ . In order to keep the continuity of the pressure and of the normal velocity across the interface, transmission conditions also need to be met. The conditions can be seen in **Eq. 2-4**:

$$u = v, \quad \frac{1}{\rho} \frac{\partial u}{\partial \nu} = \frac{1}{\rho_D} \frac{\partial v}{\partial \nu}. \quad \text{Eq. 2-4}$$

Arnold Sommerfeld defined the condition of radiation for a scalar field satisfying the Helmholtz function in 1912, which can be described mathematically as **Eq. 2-5**:

$$\lim_{r \rightarrow \infty} r \left( \frac{\partial u^s}{\partial r} - ik u^s \right) = 0, \quad r = |x|. \quad \text{Eq. 2-5}$$

The sommerfeld radiation condition is used to ensure the uniqueness for the solutions to the scattering problems. If we consider a point source  $x_0$  in three dimensions, the function  $f$ , presenting the bounded source of energy, is written as  $f(x) = \delta(x - x_0)$  in the Helmholtz equation.  $\delta$  is the Dirac delta function. Then the only solution that satisfies the Sommerfeld radiation condition is

$$\Phi(x, y) = \frac{e^{ik|x-y|}}{4\pi|x-y|}. \quad \text{Eq. 2-6}$$

This is Green's function, the fundamental solution of the Helmholtz equation.

Below, we briefly explain the layer approach in [1] that solves the direct scattering problem for smooth targets. The solution of the Helmholtz equation is  $u$  by finding the density  $\varphi$  in the layer potential. First, observe the single- and double-layer potential.

Given a function  $\varphi \in C(\partial\Omega)$ , the function

$$u(x) = \int_{\partial D} \varphi(y) \Phi(x, y) ds(y), \quad \text{Eq. 2-7}$$

is called the acoustic single-layer potential with density  $\varphi$ . The function

$$u(x) = \int_{\partial D} \varphi(y) \frac{\partial \Phi(x, y)}{\partial \nu(y)} ds(y), \quad \text{Eq. 2-8}$$

is called the acoustic double-layer potential with density  $\varphi$ . We assume to unite normal  $\nu$  to be directed into the exterior domain  $\mathbb{R}^2 \setminus \partial D$ . We note that the double-layer potential  $u$  is also a solution to the Helmholtz equation.

These two potentials are solutions to the Helmholtz equation in  $D$  and in  $\mathbb{R}^2 \setminus \partial D$ . Meanwhile, they also satisfy the Sommerfeld radiation condition. Green's formulas show that any solution of the Helmholtz equation can be represented as a combination of single- and double-layer potential.

Assume we have continuous densities  $\varphi$ . The behavior of the surface potential at the boundary is described as "jump relations". We have the following theorem from [1]:

**Theorem:** Let  $\partial D$  be of class  $C^2$  and let  $\varphi$  be continuous. Then the single-layer potential  $u$  with density  $\varphi$  is continuous throughout  $\mathbb{R}^3$  and

$$\|u\|_{\infty, \mathbb{R}^3} \leq C \|\varphi\|_{\infty, \partial D},$$

for some constant  $C$  depending on  $\partial D$ . On the boundary, we have

$$u(x) = \int_{\partial D} \varphi(y) \Phi(x, y) ds(y), \quad x \in \partial D,$$

$$\frac{\partial u_{\pm}}{\partial \nu}(x) = \int_{\partial D} \varphi(y) \frac{\partial \Phi(x, y)}{\partial \nu(y)} ds(y) \mp \frac{1}{2} \varphi(x), \quad x \in \partial D,$$

where

$$\frac{\partial u_{\pm}}{\partial \nu}(x) := \lim_{h \rightarrow +0} \nu(x) \cdot \text{grad } u(x \pm h\nu(x)),$$

is to be understood in the sense of uniform convergence on  $\partial D$  and where the integral exists as improper integrals. The double-layer potential  $v$  with density  $\varphi$  can be continuously extended from  $D$  to  $\bar{D}$  and from  $\mathbb{R}^3 \setminus \bar{D}$  to  $\mathbb{R}^3 \setminus D$  with limiting values

$$v_{\pm}(x) = \int_{\partial D} \varphi(y) \frac{\partial \Phi(x, y)}{\partial \nu(y)} ds(y) \pm \frac{1}{2} \varphi(x), \quad x \in \partial D,$$

where

$$v_{\pm}(x) := \lim_{h \rightarrow +0} \nu(x \pm h\nu(x)),$$

and where the integral exists as an improper integral. Furthermore,

$$\|u\|_{\infty, D} \leq C \|\varphi\|_{\infty, \partial D},$$

$$\|u\|_{\infty, \mathbb{R}^3 \setminus D} \leq C \|\varphi\|_{\infty, \partial D},$$

for some constant  $C$  depending on  $\partial D$  and

$$\lim_{h \rightarrow +0} \left\{ \frac{\partial v}{\partial \nu}(x + h\nu(x)) - \frac{\partial v}{\partial \nu}(x - h\nu(x)) \right\} = 0, \quad x \in \partial D,$$

uniformly on  $\partial D$ .

Based on the above theorem, our single layer potential takes the same form on the boundary:

$$u_1(x) = \int_{\partial D} \varphi(y) \Phi(x, y) ds(y), \quad x \in \partial D.$$

**Eq. 2-9**

However, the double-layer potential is changed to

$$u_2(x) = \int_{\partial D} \varphi(y) \frac{\partial \Phi(x, y)}{\partial \nu(y)} ds(y) + \frac{1}{2} \varphi(x), \quad x \in \partial D. \quad \text{Eq. 2-10}$$

We define the single- and double-layer operators  $S$  and  $K$ , which can be described as

$$(S\varphi)(x) = 2 \int_{\partial D} \Phi(x, y) \varphi(y) ds(y), \quad x \in \partial D, \quad \text{Eq. 2-11}$$

$$(K\varphi)(x) = 2 \int_{\partial D} \frac{\partial \Phi(x, y)}{\partial \nu(y)} \varphi(y) ds(y), \quad x \in \partial D. \quad \text{Eq. 2-12}$$

The existence of the solution of the exterior Dirichlet problem is based on boundary integral equations. In the method “layer approach”, we choose the combined single- and double-layer potential approach so that the integral equation is uniquely solvable. The approach is represented as

$$u(x) = \int_{\partial D} \left\{ \frac{\partial \Phi(x, y)}{\partial \nu(y)} - i\eta \Phi(x, y) \right\} \varphi(y) ds(y), \quad x \in \mathbb{R}^2 \setminus \partial D, \quad \text{Eq. 2-13}$$

where  $\eta$  is a coupling parameter.

Combining the operators  $S$ ,  $K$  (Eq. 2-11 and Eq. 2-12) and the jump relation (Eq. 2-10), the approach can be rewritten in the form of

$$\varphi + K\varphi - i\eta S\varphi = 2f, \quad x \in \partial D. \quad \text{Eq. 2-14}$$

In order to find the numerical solution in 2D, rewrite the above equation in parametric form:

$$\psi(t) - \int_0^{2\pi} \{L(t, \tau) + i\eta M(t, \tau)\} \psi(\tau) d\tau = g(t), \quad 0 \leq t \leq 2\pi, \quad \text{Eq. 2-15}$$

where

$$\psi(t) = \varphi(x(t)), \quad g(t) = 2f(x(t)).$$

The kernels are given by

$$L(t, \tau) := \frac{ik}{2} \{x_2'(\tau)[x_1(\tau) - x_1(t)] - x_1'(\tau)[x_2(\tau) - x_2(t)]\} \frac{H_1^{(1)}(kr(t, \tau))}{r(t, \tau)},$$

$$M(t, \tau) := \frac{i}{2} H_0^{(1)}(kr(t, \tau)) \{[x_1'(\tau)]^2 + [x_2'(\tau)]^2\}^{1/2}.$$

Note that  $\Phi(x, y) := \frac{i}{4} H_0^{(1)}(kr)$ , for  $t \neq \tau$ , we have the set

$$r(t, \tau) := \{[x_1(t) - x_1(\tau)]^2 + [x_2(t) - x_2(\tau)]^2\}^{1/2}. \quad \text{Eq. 2-16}$$

From the expansion for the Neumann functions [1], we see that the kernels L and M have logarithmic singularities at  $t = \tau$ . Hence, for their proper numerical treatment, following Martensen [2] and Kussmaul [3], we split the kernels into

$$L(t, \tau) = L_1(t, \tau) \ln(4 \sin^2 \frac{t - \tau}{2}) + L_2(t, \tau), \quad \text{Eq. 2-17}$$

$$M(t, \tau) = M_1(t, \tau) \ln(4 \sin^2 \frac{t - \tau}{2}) + M_2(t, \tau), \quad \text{Eq. 2-18}$$

where

$$L_1(t, \tau) := \frac{k}{2\pi} \{x_2'(\tau)[x_1(t) - x_1(\tau)] - x_1'(\tau)[x_2(t) - x_2(\tau)]\} \frac{J_1(kr(t, \tau))}{r(t, \tau)},$$

$$L_2(t, \tau) := L(t, \tau) - L_1(t, \tau) \ln(4 \sin^2 \frac{t - \tau}{2}),$$

$$M_1(t, \tau) := -\frac{1}{2\pi} J_0(kr(t, \tau) \{[x'_1(\tau)]^2 + [x'_2(\tau)]^2\}^{1/2},$$

$$M_2(t, \tau) := M(t, \tau) - M_1(t, \tau) \ln(4 \sin^2 \frac{t-\tau}{2}).$$

The kernels  $L_1, L_2, M_1$  and  $M_2$  turn out to be analytic. Use Bessel's functions of order  $n$ . We can reduce the diagonal terms as

$$L_2(t, t) = L(t, t) = \frac{1}{2\pi} \frac{x'_1(t)x''_2(t) - x'_2(t)x''_1(t)}{[x'_1(t)]^2 + [x'_2(t)]^2},$$

$$M_2(t, t) = \left\{ \frac{i}{2} - \frac{C}{\pi} - \frac{1}{2\pi} \ln \left( \frac{k^2}{4} \{[x'_1(t)]^2 + [x'_2(t)]^2\} \right) \right\} \{[x'_1(t)]^2 + [x'_2(t)]^2\}^{\frac{1}{2}},$$

where the Euler constant is  $C = 0.57721566$ .

Despite the continuity of kernel  $L$ , it is good to separate the logarithm part of  $L$  since the derivatives of  $L$  fail to be continuous at

$$\psi(t) - \int_0^{2\pi} K(t, \tau)\psi(\tau)d\tau = g(t), \quad 0 \leq t \leq 2\pi, \quad \text{Eq. 2-19}$$

where the kernel  $K$  is:

$$K(t, \tau) := K_1(t, \tau) \ln(4 \sin^2 \frac{t-\tau}{2}) + K_2(t, \tau).$$

There are three basic numerical methods of integral equations of the second kind: Nystrom, collocation and the Galerkin method. The Nystrom method is more practical when we deal with 1D or 2D problem because this method requires less computational effort. The Nystrom method only evaluates the kernel function for the evaluation of each of the matrix elements of the linear system. This method consists of the straightforward

approximation of the integrals by quadrature formulas using the quadrature rule:

$$\int_0^{2\pi} \ln\left(4 \sin^2 \frac{t-\tau}{2}\right) f(\tau) d\tau \approx \sum_{j=0}^{2n-1} R_j^{(n)}(t) f(t_j), \quad 0 \leq t \leq 2\pi, \quad \text{Eq. 2-20}$$

with quadrature weights given by

$$R_j^{(n)}(t) := -\frac{2\pi}{n} \sum_{m=1}^{n-1} \frac{1}{m} \cos m(t-t_j) - \frac{\pi}{n^2} \cos n(t-t_j), \quad j = 0, \dots, 2n-1,$$

and the trapezoidal rule:

$$\int_0^{2\pi} f(\tau) d\tau \approx \frac{\pi}{n} \sum_{j=0}^{2n-1} f(t_j). \quad \text{Eq. 2-21}$$

The integral equation is replaced by the approximating equation:

$$\psi^{(n)}(t) - \sum_{j=0}^{2n-1} \left\{ R_j^{(n)}(t) K_1(t, t_j) + \frac{\pi}{n} K_2(t, t_j) \right\} \psi^{(n)}(t_j) = g(t). \quad \text{Eq. 2-22}$$

The solution of **Eq. 2-22** reduces to solving a finite dimensional linear system.

For any solution from **Eq. 2-22**, the values  $\psi_i^{(n)} = \psi^{(n)}(t_i)$ ,  $i = 0, \dots, 2n-1$ , at the

quadrature points trivially satisfy the linear system:

$$\psi_i^{(n)} - \sum_{j=0}^{2n-1} \left\{ R_{|i-j|}^{(n)} K_1(t_i, t_j) + \frac{\pi}{n} K_2(t_i, t_j) \right\} \psi_j^{(n)} = g(t_i), \quad \text{Eq. 2-23}$$

where

$$R_j^{(n)} := R_j^{(n)}(0) = -\frac{2\pi}{n} \sum_{m=1}^{n-1} \frac{1}{m} \cos \frac{mj\pi}{n} - \frac{(-1)^j \pi}{n^2}, \quad j = 0, \dots, 2n-1,$$

which means the solution can be defined as

$$\psi^{(n)}(t) := \sum_{j=0}^{2n-1} \left\{ R_j^{(n)}(t) K_1(t, t_j) + \frac{\pi}{n} K_2(t, t_j) \right\} \psi_j^{(n)} + g(t). \quad \text{Eq. 2-24}$$

For the far field we have the formula:

$$u_\infty(\hat{x}) = -\frac{e^{i\pi/4}}{\sqrt{8\pi k}} \int_{\partial\Omega} \{k\nu(y) \cdot \hat{x} + \eta\} e^{-ik\hat{x}\cdot y} \varphi(y) ds(y), \quad |\hat{x}| = 1,$$

and the near field we have the formula:

$$u(x) = \int_{\partial D} \left\{ \frac{\partial\Phi(x, y)}{\partial\nu(y)} - i\eta\Phi(x, y) \right\} \varphi(y) ds(y), \quad x \in \mathbb{R}^2 \setminus \partial D.$$

Provided the integral equation Eq. 2-19 itself is uniquely solvable and the kernels  $K_1$  and  $K_2$  and the right hand side  $g$  are continuous, a complicated error analysis shows that

1. The approximating linear system **Eq. 2-23**, i.e., the approximating equation **Eq. 2-22**, is uniquely solvable for all sufficiently large  $n$ ;
2. As  $n \rightarrow \infty$ , the approximate solutions  $\psi^{(n)}$  converge uniformly to the solution  $\psi$  of the integral equation;
3. The convergence order of the quadrature errors for **Eq. 2-20** and **Eq. 2-21** carries over to the error  $\psi^{(n)} - \psi$ .

The latter means that in the case of analytic kernels  $K_1$  and  $K_2$  and analytic right hand sides  $g$ , the approximation error decreases exponentially, i.e., there exist positive

constants  $C$  and  $\sigma$  such that

$$|\psi^{(n)}(t) - \psi(t)| \leq Ce^{-n\sigma}, \quad 0 \leq t \leq 2\pi,$$

for all  $n$ . This is exponential convergence.

The above discussion is for smooth targets. Our research is focused on non-smooth targets with multiple corners. It will be described in the next chapter.

## 2.2 The Inverse Scattering Problem

The inverse problem has progressed since the 1980's. In most cases, the inverse scattering problem is inherently nonlinear and, more seriously from the point of view of numerical computations, improperly posed. As a result of this, recovering the refractive index  $n(x)$  in the whole domain is a difficult task.

Here, if we consider the target medium is homogeneous, the  $n(x)$  is a constant inside the target. Then we can turn the inverse problem into a geometric problem by reconstructing the shape of the target.

Inverse scattering problem is widely used in the industry such as: underground mine detection, target detection using radar or sonar system, ultrasound imaging, and reflection seismology. There are two main types of numerical method for the inverse problem: the direct imaging method and the iterative method.

In the iterative method, the boundary of the target is updated to minimize the residual of the scattered field. Well-known methods are the Newton method, the Landweber method and least square fits. These methods use the model of the full forward problem for the solution of the inverse problem. Because these techniques take advantage of all the information about the forward problem, they usually get quite good

reconstructions. However, due to the fact that they are required to solve the forward problem many times for information, the iterative method is computationally intensive. What is more, it is difficult to obtain a localized reconstruction in a limited problematic data setting.

In the direct imaging method, the geometry of the target is given by designing an imaging function based on the response matrix. This is the most recent class of algorithms for the inverse problem. The most significant advantage of these techniques is that they can be applied without knowing whether the scatterer is impenetrable, or it is an inhomogeneous medium.

Decomposition algorithms consist of the methods that split the inverse problem into an ill-posed part to reconstruct the scattered field and a well-posed part to find the unknown scatterer due to the boundary condition. Well known method includes dual space method [4,5], the technique of Kirsch and Kress [1] and the point source method of Potthast [7,8,9].

The linear sampling method, first proposed in [42], is one of the direct imaging algorithms for inverse problems. This method is based on a characterization of the range of the scattering operator for the far field pattern. The far field pattern of a point source located inside the object should be in the range of the scattering operator.

The domain of an unknown scatterer by the behavior of the solution to the integral equation is

$$\int_s u_\infty(\hat{x}, \hat{y}) g(\hat{y}) ds(\hat{y}) = e^{ik\hat{x} \cdot z}, \quad \hat{x} \in \mathbb{S}.$$

Kirsch then developed a factorization of the scattering operator and uses it for imaging:

$$(Fg)(\hat{x}) := \int_s u^\infty(\hat{x}, \hat{y})g(\hat{y})ds(\hat{y}), \quad \hat{x} \in \mathbb{S}.$$

By using the operator, Kirsch proposed to solve the equation

$$(F^*F)^{1/4}g(\hat{x}) = e^{ik\hat{x}\cdot z}, \quad \hat{x} \in \mathbb{S}.$$

For all  $z$  on the sampling grid, the equation is solvable if and only if  $z$  is the interior of the unknown scatterer.

Ikehata and Potthast proposed two independent related algorithms, the probe method [10] and the method of singular source [9]. These methods are different from the linear sampling method of Kirsch because they use different quantities that blow up when approaching the boundaries of some scatterers. The probe method of Ikehata uses Green's function to define an indicator function. This indicator function blows up when the virtual source touches the targeted obstacle. The singular sources method of Potthast uses a different functional that blows up at the boundary of the obstacle. However the basic concepts of these two methods are the same.

After the probe method, Ikehata's developed enclosure method [11, 12] enables us to use very limited data to finish the reconstruction process. He uses a special harmonic incident field:

$$v = e^{\tau x \cdot (\omega + i\omega^\perp)}.$$

To construct the indicator function:

$$I_\omega(\tau, t) = e^{-\tau t} \left\{ \left\langle \frac{\partial u}{\partial \nu} \Big|_{\partial G}, v \Big|_{\partial G} \right\rangle - \left\langle \frac{\partial u}{\partial \nu} \Big|_{\partial G}, u \Big|_{\partial G} \right\rangle \right\}, \quad \tau > 0, \quad t \in \mathbb{R},$$

where  $\omega$  a direction vector,  $u$  is the unknown solution, and  $G$  is some domain containing the unknown scatterer. Ikehata shows that at the corners of polygonal scatterers, this

function becomes unbounded. Then he exploits this property to uniquely reconstruct the scatterer. The enclosure method is a method independent of the material properties of the scatterer.

Luke and Potthast developed another technique for locating a scatterer from a single incident wave that also exploits the behavior of a special indicator function in the neighborhood of a scatterer. The method is called the no response test. Compared to the enclosure method, the no response test does not make use of, nor place any particular constraints on, the geometric properties of the scatterer.

MUSIC algorithm is a method of characterizing the range of a self-adjoint operator. MUSIC is an abbreviation for multiple signal classification. Because we know a self-adjoint matrix  $A$ 's noise subspace is orthogonal to the range. If a vector  $\vec{f}$  is in the range, its projection onto the noise subspace is zero. This is the basic idea of MUSIC algorithm.

With full provided aperture data given, the generalized MUSIC algorithm for a single frequency is capable of imaging different types of targets with efficiency, robustness and accuracy. However, the results are typically not very good for limited aperture. Multiple frequencies should be used to complement the lack of spatial aperture. The MUSIC algorithm is based on the singular value decomposition of the response matrix. We know that this decomposition allows for an arbitrary complex phase. As a result of that, combining different frequencies in a phase coherent way is not direct.

In [27], multi-tone imaging algorithm is introduced to make use of coherent information in both phase and space. This multi-tone algorithm takes the advantage of

phase coherence from multiple frequency data to improve both resolution of robustness of the imaging procedure. There are two crucial points in the multi-tone algorithm.

1. Physically based factorization of the response matrix that transforms a passive target detection problem to an active source detection problem.
2. A phase coherent imaging function that can superpose multiple tones and multiple frequencies to take advantage of both spatial diversity of the array and/or the bandwidth of the probing signal.

This multi-tone method is simple and efficient because no forward solver or iteration is needed. Because this method takes advantage of multiple frequencies, the imaging is enhanced and it is robust with respect to noise. Thus, this method can deal with limited or synthetic aperture data naturally as well as with different material properties and different types of illuminations and measurements.

The general inverse problem approach to the whole medium is regarded as the unknown. That means an inverse or pseudo-inverse of the forward operator has to be approximated and computed. The inverse problem is also nonlinear even if the forward problem is linear in most cases. Iterations are required to solve this kind of nonlinear optimization problem. It also involves solving an adjoint forward problem at each iteration. What is more, the inverse problem is often ill-posed and regularization has to be introduced. Thus, imaging the whole medium using the general inverse problem approach may be too complicated and too expensive to be practical in the applications if there exists a large imaging domain.

In [25], Hou found that if the background medium is homogeneous and some simple boundary condition is satisfied at the boundary of the target, the inverse problem

can be turned into a geometric problem. This means that it changes to a problem of determining the shape of the target from the scattered wave field pattern. In this case, the number of degrees of freedom will be greatly reduced from imaging the whole medium.

As just discussed the inverse medium scattering problems have two major difficulties: the ill-posedness and the presence of many local minima. To overcome these difficulties, stable and efficient regularized recursive linearization methods are developed in [15, 16, 17, 18] for solving the 2D Helmholtz equation and the 3D Maxwell's equation [19, 20] in the case of full aperture data. These methods start from the weak scattering, where Born approximation may be used to produce initial guesses. Even if the methods yield stable and accurate computational results, they nonetheless rely on the weak scattering assumption for initial guesses. Unfortunately, if the weak scattering assumption is violated, the Born approximation might lead to an initial guess with which the continuation approach would converge slowly or even diverge. To solve the problem which Born approximation may not be valid, [29] proposed a continuation approach starting from an initial guess via the MUSIC algorithm and a level set representation at a fixed wave number. The method requires multiple frequencies scattering data and the recursive linearization is a continuation procedure on the wave numbers.

In [25], a very important algorithm is introduced. The algorithm is based on a physical factorization of the response matrix of a transducer array and the MUSIC imaging function is used to visualize the result. This algorithm is simple and efficient since no forward solver or iteration is needed and multiple-frequency information improves both resolution and stability of the algorithm.

The direct imaging algorithm in [25] can image both location and geometry of extended targets. The motivation of this method is to locate or visualize dominant scattering events. In homogeneous media, this is equivalent to finding the boundary of a target that has some contrast from the background. For heterogeneous media, whether this method can clearly locate or visualize the boundary depends on two factors:

1. To what extent the scattering at the boundary of the target dominates other scattering events in the medium.
2. Knowledge about the background medium. With a physically based thresholding, this direct imaging algorithm can deal with quite strong measurement noise.

This direct imaging method's physical model is the Helmholtz equation for harmonic waves. An array of transducers that can send out waves and record scattered waves is used to probe the medium. The response matrix is built by the measurement data. This response matrix contains all the information about the medium that can be obtained with the transducer array. Based on a physical factorization of the scattered field, the Singular Value Decomposition (SVD) is characterized for extended targets. A direct imaging function based on the SVD then is designed and a thresholding strategy for regularization based on the physical resolution of the array and the noise level is introduced.

Another physical motivation of the algorithm is that strong scattering events can be considered as sources for the scattered field. In time reversal, the received wave field is time reversed and back propagated into the medium. Then the retransmitted wave will focus on the sources. If we want to detect a target, the target is illuminated by a probing wave first, and then the time reversed wave will focus on dominant scatterers. However,

the standard time reversal procedure can only locate the most dominant scattering event associated with the largest singular value or dominant events associated with different singular values one by one. As a result of that, for an extended target, we need to use the SVD to extract the dominant events that characterize the information of the shape.

The imaging function is a similar form as the MUSIC imaging function. The MUSIC algorithm can only locate a small target. However, for extended targets, the response matrix has a more complicated structure. In order to locate an extended target, a physical representation of the scattered field and the corresponding response matrix is produced. Then a thresholding strategy is also developed based on the resolution of the array and the SVD of the response matrix. Using these two ideas, important contributions to the scattered field simultaneously from the SVD of the response matrix can be extracted.

It should be noticed that this algorithm is different from the algorithm in [22]. In [22], the method is using a shape optimization to match all measurements in the response matrix.

## CHAPTER 3

### METHODS

In this chapter, we propose forward and inverse problem solvers from domains with multiple corners. For the forward problem, the work introduced in the previous chapter is for the smooth target case. We will first discuss the idea in [1] for domains with one corner. Then we will explain our improvement to treat domains with multiple corners. For the inverse problem, we will discuss how to use MUSIC and other direct imaging algorithms to solve the inverse problem for domains with multiple corners. This research work is published in [43].

#### 3.1 The Forward Problem

Consider a time-harmonic plane wave,  $u^i = e^{ikx \cdot d}$ , incident on a scatterer  $\Omega \in \mathbb{R}^2$  with multiple corners, where  $k$  is the wave number and  $d \in S^1$  is the incident direction. Let  $\partial\Omega$  be the boundary of the scatterer. We consider the obstacle scattering problem. The total field  $u$  satisfies the Helmholtz equation:

$$\Delta u + k^2 u = 0 \quad \text{in } \mathbb{R}^2 \setminus \bar{\Omega}, \quad \text{Eq. 3-1}$$

$$u = 0 \quad \text{on } \partial\Omega. \quad \text{Eq. 3-2}$$

The total field consists of the incident field and the scattered field

$$u = u^i + u^s. \quad \text{Eq. 3-3}$$

The incident field satisfies the homogeneous equation:

$$\Delta u^i + k^2 u^i = 0. \quad \text{Eq. 3-4}$$

It follows from Eq. 3-1 to Eq. 3-3 that the scattered field satisfies

$$\Delta u^s + k^2 u^s = 0 \quad \text{in } \mathbb{R}^2 \setminus \bar{\Omega}, \quad \text{Eq. 3-5}$$

$$u^s = -u^i \quad \text{on } \partial\Omega. \quad \text{Eq. 3-6}$$

In addition, the scattered field is required to satisfy the following Sommerfeld radiation condition

$$\lim_{r \rightarrow \infty} \sqrt{r} \left( \frac{\partial u^s}{\partial r} - ik u^s \right) = 0, \quad r = |x|, \quad \text{Eq. 3-7}$$

uniformly in  $x/|x|$ . The uniqueness of the solution to the obstacle scattering problem is discussed in [1].

Given a function  $\varphi \in C(\partial\Omega)$ , the function

$$u(x) = \int_{\partial D} \varphi(y) \Phi(x, y) ds(y), \quad \text{Eq. 3-8}$$

is called the acoustic single-layer potential with density  $\varphi$ . Since for  $x \in \mathbb{R}^2 \setminus \partial D$ , we can differentiate under the integral sign. The solution of the Helmholtz equation is  $u$ .

The function

$$v(x) = \int_{\partial D} \varphi(y) \frac{\partial \Phi(x, y)}{\partial \nu(y)} ds(y), \quad \text{Eq. 3-9}$$

is called the acoustic double-layer potential with density  $\varphi$ . We assume to unite normal  $\nu$  to be directed into the exterior domain  $\mathbb{R}^2 \setminus \partial D$ . We note that the double-layer potential  $u$  is also a solution to the Helmholtz equation.

We use the combined single- and double-layer potential approach [23] so that the integral equation is uniquely solvable. For simplicity of notation, we first assume there is one corner at  $x_0$  then

$$u(x) = \int_{\partial D} \left[ \left\{ \frac{\partial \Phi(x, y)}{\partial \nu(y)} - i\eta \Phi(x, y) \right\} \varphi(y) - \frac{\partial \Phi_0(x, y)}{\partial \nu(y)} \varphi(x_0) \right] ds(y), \quad \text{Eq. 3-10}$$

$$\Phi_0(x, y) := \frac{1}{2\pi} \ln \frac{1}{|x - y|}, \quad x \neq y, \quad \text{Eq. 3-11}$$

$$\Phi(x, y) := \begin{cases} \frac{i}{4} H_0^{(1)}(k|x - y|), & d = 2 \\ \frac{e^{ik|x - y|}}{4\pi|x - y|}, & d = 3. \end{cases} \quad \text{Eq. 3-12}$$

By using the jump relation [1], we have the integral equation

$$\begin{aligned} \varphi(x) - \varphi(x_0) + 2 \int_{\partial D} \left\{ \frac{\partial \Phi(x, y)}{\partial \nu(y)} - i\eta \Phi(x, y) \right\} \varphi(y) ds(y) \\ - 2 \int_{\partial D} \frac{\partial \Phi_0(x, y)}{\partial \nu(y)} \varphi(x_0) ds(y) = 2f(x), \quad x \in \partial D. \end{aligned} \quad \text{Eq. 3-13}$$

We use the change of variable and trapezoidal rule as follows [1]. Roughly speaking, about half of the points are equally distributed while the other half is accumulated near the corner

$$\int_0^{2\pi} f(t) dt = \int_0^{2\pi} w'(s) f(w(s)) ds, \quad \text{Eq. 3-14}$$

$$\int_0^{2\pi} f(t) dt \approx \frac{\pi}{n} \sum_{j=0}^{2n-1} a_j f(s_j), \quad \text{Eq. 3-15}$$

$$a_j = w'\left(\frac{j\pi}{n}\right), \quad s_j = w\left(\frac{j\pi}{n}\right), \quad j = 1, \dots, 2n - 1, \quad \text{Eq. 3-16}$$

$$w(s) = 2\pi \frac{[v(s)]^p}{[v(s)]^p + [v(2\pi - s)]^p}, \quad 0 \leq s \leq 2\pi, \quad \text{Eq. 3-17}$$

$$v(s) = \left(\frac{1}{p} - \frac{1}{2}\right) \left(\frac{\pi - s}{\pi}\right)^3 + \frac{1}{p} \frac{s - \pi}{\pi} + \frac{1}{2}, \quad \text{Eq. 3-18}$$

where we use  $p = 8$  in our numerical experiments.

We define:

$$H(t, \tau) = \begin{cases} \frac{1}{\pi} \frac{x_2'(\tau)[x_1(t) - x_1(\tau)] - x_1'(\tau)[x_2(t) - x_2(\tau)]}{[x_1(t) - x_1(\tau)]^2 + [x_2(t) - x_2(\tau)]^2}, & t \neq \tau, \\ \frac{1}{2\pi} \frac{x_2'(t)x_1''(t) - x_1'(t)x_2''(t)}{[x_1'(t)]^2 + [x_2'(t)]^2}, & t = \tau, t \neq 0, 2\pi. \end{cases} \quad \text{Eq. 3-19}$$

We set  $t = w(s)$  and  $\tau = w(\sigma)$  to obtain

$$K(w(s), w(\sigma)) = \tilde{K}_1(s, \sigma) \ln\left(4 \sin^2 \frac{s - \sigma}{2}\right) + \tilde{K}_2(s, \sigma), \quad \text{Eq. 3-20}$$

where

$$\tilde{K}_1(s, \sigma) = K_1(w(s), w(\sigma)), \quad \text{Eq. 3-21}$$

$$K_2(s, s) = \lim_{\sigma \rightarrow s} [K(s, \sigma) - K_1(s, \sigma) \ln\left(4 \sin^2 \frac{s - \sigma}{2}\right)], \quad \text{Eq. 3-22}$$

$$\tilde{K}_2(s, \sigma) = K(w(s), w(\sigma)) - \tilde{K}_1(s, \sigma) \ln\left(4 \sin^2 \frac{s - \sigma}{2}\right), \quad s \neq \sigma, \quad \text{Eq. 3-23}$$

$$\tilde{K}_2(s, s) = K_2(w(s), w(s)) + 2 \ln w'(s) K_1(w(s), w(s)). \quad \text{Eq. 3-24}$$

These lead to a linear system

$$\begin{aligned} \psi_i^{(n)} - \psi_0^{(n)} - \sum_{j=1}^{2n-1} \left\{ R_{|i-j|}^{(n)} \tilde{K}_1(s_i, s_j) + \frac{\pi}{n} \tilde{K}_2(s_i, s_j) \right\} a_j \psi_j^{(n)} \\ - \sum_{j=1}^{2n-1} \frac{\pi}{n} H(s_i, s_j) a_j \psi_0^{(n)} = g(s_i), \quad i = 0, \dots, 2n-1. \end{aligned} \quad \text{Eq. 3-25}$$

The condition number is an important concept for linear systems. It is defined as

$$\kappa(A) = \|A\| \|A^{-1}\|. \quad \text{Eq. 3-26}$$

If the condition number is large, then a small change in the data could lead to a large change in the solution of a linear system with the coefficient matrix  $A$ .

In [1], the algorithm using graded mesh for solving direct scattering problem for sound-soft obstacle with one corner is presented. However, if we follow the same steps to treat the problem with multiple corners, large condition number for the linear system is observed (see Section 4.1). We propose a method to reduce the condition number. In [1], a notationally advantageous modification is made to the integral equation by inserting terms involving the fundamental solution to the Laplace equation. We observed that if this particular modification is not made, then the condition number is reduced significantly (see Section 4.1).

The right hand side of the linear system  $g$  depends on the incident field. We could have plane incident wave or have a point source. These give two possibilities. From the solution to the linear system (the density function), we could integrate and obtain both the near field data and the far field data. These also give two possibilities. Overall, there are four possibilities as follows:

1. Plane incident wave, far field data
2. Plane incident wave, near field data
3. Point source, far field data
4. Point source, near field data

The following formulas show the data for the four cases:

The formula for far field data is

$$u_{\infty}(\hat{x}) = -\frac{e^{i\pi/4}}{\sqrt{8\pi k}} \int_{\partial\Omega} \{k\nu(y) \cdot \hat{x} + \eta\} e^{-ik\hat{x} \cdot y} \varphi(y) ds(y), \quad |\hat{x}| = 1. \quad \text{Eq. 3-27}$$

The formula for near field data is

$$u(x) = \int_{\partial D} \left\{ \frac{\partial\Phi(x, y)}{\partial\nu(y)} - i\eta\Phi(x, y) \right\} \varphi(y) ds(y), \quad x \in \mathbb{R}^2 \setminus \partial D. \quad \text{Eq. 3-28}$$

We place the transducers at  $(r \cos \theta, r \sin \theta)$  for near field. Let  $y = (x_1, x_2)$  be a point on the target boundary  $\partial D$ . We have

$$x = (r \cos \theta, r \sin \theta), \quad \text{Eq. 3-29}$$

$$y = (x_1, x_2). \quad \text{Eq. 3-30}$$

Let

$$\tilde{r} = x - y = (r \cos \theta - x_1, r \sin \theta - x_2). \quad \text{Eq. 3-31}$$

The distance is

$$|x - y| = |\tilde{r}| = \sqrt{(r \cos \theta - x_1)^2 + (r \sin \theta - x_2)^2}. \quad \text{Eq. 3-32}$$

The Green's function is

$$\begin{aligned} \Phi(x, y) &= \frac{i}{4} H_0^{(1)}(k|x - y|) = \frac{i}{4} H_0^{(1)}(k\tilde{r}) \\ &= \frac{i}{4} H_0^{(1)}(k\sqrt{(r \cos \theta - x_1)^2 + (r \sin \theta - x_2)^2}). \end{aligned} \quad \text{Eq. 3-33}$$

We take the derivative and directional derivative:

$$\begin{aligned} \frac{\partial}{\partial x_1} H_0^{(1)}(k\tilde{r}) &= -H_1^{(1)}(k\sqrt{(r \cos \theta - x_1)^2 + (r \sin \theta - x_2)^2}) \\ &\cdot k \frac{x_1 - r \cos \theta}{\sqrt{(r \cos \theta - x_1)^2 + (r \sin \theta - x_2)^2}}, \end{aligned} \quad \text{Eq. 3-34}$$

$$\frac{\partial}{\partial \nu} H_0^{(1)}(k\tilde{r}) = \frac{[\nu_1(x_1 - r \cos \theta) + \nu_2(x_2 - r \sin \theta)] - k H_1^{(1)}(k\sqrt{(r \cos \theta - x_1)^2 + (r \sin \theta - x_2)^2})}{\sqrt{(r \cos \theta - x_1)^2 + (r \sin \theta - x_2)^2}}. \quad \text{Eq. 3-35}$$

with these details, we are able to compute both terms in **Eq. 3-10**. Another issue is that for point source incident instead of plan wave we replace  $e^{ikx \cdot d}$  with  $\frac{i}{4} H_0^{(1)}(k\tilde{r})$ .

Above, we discussed how to compute near field or far field data based on point source or plane incident wave. These are four cases with four response matrices:

1. P1: Plane incident wave, far field data
2. P2: Plane incident wave, near field data
3. P3: Point Source, far field data
4. P4: Point Source, near field data

We have the following response matrix relations:

$$p_1 = \frac{e^{ik\|x\|}}{\|x\|^{\frac{d-1}{2}}} (p_2 + O(\frac{1}{\|x\|})), \quad \text{Eq. 3-36}$$

$$p_3 = \frac{e^{ik\|x\|}}{\|x\|^{\frac{d-1}{2}}} (p_4 + O(\frac{1}{\|x\|})), \quad \text{Eq. 3-37}$$

$$p_2 = \beta p_3^T. \quad \text{Eq. 3-38}$$

$$\text{For } 3D : \beta = \frac{1}{4\pi}, \text{ For } 2D : \beta = \frac{e^{i\pi/4}}{\sqrt{8\pi k}}.$$

The corresponding singular values of the response matrices have the relations

$$\sigma_{i,1} \approx \frac{1}{\sqrt{r}} \sigma_{i,2}, \quad \text{Eq. 3-39}$$

$$\sigma_{i,2} = \frac{1}{\sqrt{8\pi k}} \sigma_{i,3}, \quad \text{Eq. 3-40}$$

$$\sigma_{i,3} \approx \frac{1}{\sqrt{r}} \sigma_{i,4}. \quad \text{Eq. 3-41}$$

In fact,  $\sigma_{1,1} > \frac{1}{\sqrt{r}} \sigma_{1,2}$ ,  $\sigma_{i,3} > \frac{1}{\sqrt{r}} \sigma_{i,4}$  because the singular value perturbation tends to have a bias to be larger with an unbiased perturbation of the matrix. The explanation is in Section 3.2. We will verify these relations numerically in Section 4.1.

### 3.2 The Inverse Problem

Shape reconstruction has important applications in radar, sonar, and geophysical exploration, in medical imaging, and in nondestructive testing [1]. The nonlinearity and illposedness make it a challenging problem. There are two types of methods for solving the problem. The direct methods [24, 25, 26, 27, 28] are efficient but less accurate; the iterative methods [20, 22, 29, 31, 32, 33, 34, 35, 36] are accurate but more expensive. Typically, the forward and adjoint problems have to be solved in each iteration.

**Figure 3-1** shows a typical configuration for such a problem. The background medium is assumed to be homogeneous.

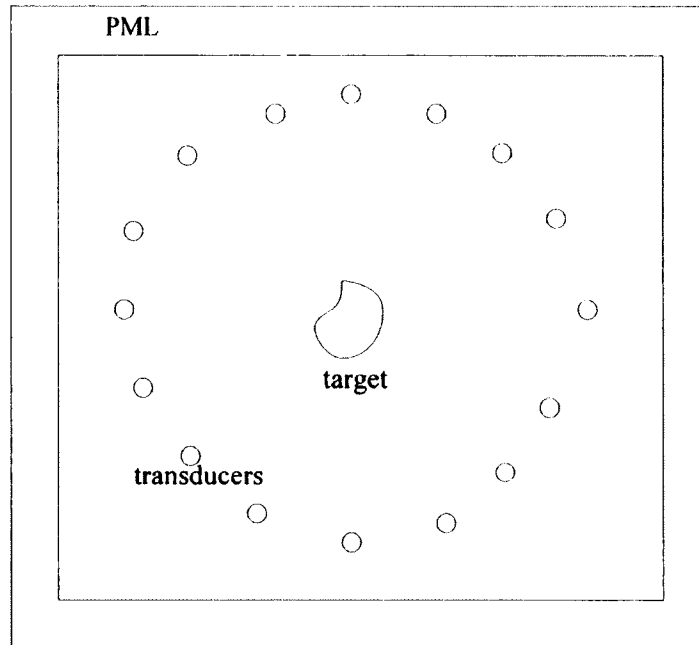


**Figure 3-1:** Setup for Inverse Problems.

The response matrix is a collection of the scattered field data received at the  $j^{th}$  transducer which originated at the  $i^{th}$  transducer. There are two ways to obtain data for the response matrix. One is to do physical measurements. The other is to solve the forward problem given the target shapes. One way to solve for the scattered field is to truncate the unbounded domain to a bounded domain using the perfectly matched layer (PML) technique [39, 40]. This layer is shown in **Figure 3-1**. In this dissertation, we use our forward solver in Section 3.1 using a boundary integral formulation. As we discussed earlier, we expect our forward solver to have slower than exponential convergence, but accurate enough to use as input data for inverse problems.

The response matrix is complex symmetric due to the reciprocity relation in [1] below:

**Theorem.** The far field pattern for sound-soft obstacle scattering satisfies the reciprocity relation

$$u_\infty(\hat{x}; d) = u_\infty(-d; -\hat{x}), \quad \hat{x}, d \in \Omega. \quad \text{Eq. 3-42}$$

**Proof.** By Green's theorem, the Helmholtz equation for the incident and the scattered wave and the radiation condition for the scattered wave we find

$$\int_{\partial D} \left\{ u^i(\cdot; d) \frac{\partial}{\partial \nu} u^i(\cdot; -\hat{x}) - u^i(\cdot; -\hat{x}) \frac{\partial}{\partial \nu} u^i(\cdot; d) \right\} ds = 0,$$

and

$$\int_{\partial D} \left\{ u^s(\cdot; d) \frac{\partial}{\partial \nu} u^s(\cdot; -\hat{x}) - u^s(\cdot; -\hat{x}) \frac{\partial}{\partial \nu} u^s(\cdot; d) \right\} ds = 0.$$

We have

$$u_\infty(\hat{x}) = \frac{1}{4\pi} \int_{\partial D} \left\{ u(y) \frac{\partial e^{-ik\hat{x}\cdot y}}{\partial \nu(y)} - \frac{\partial u}{\partial \nu}(y) e^{-ik\hat{x}\cdot y} \right\} ds(y), \quad \hat{x} \in \Omega.$$

It can be deduced that

$$4\pi u_\infty(\hat{x}; d) = \int_{\partial D} \left\{ u^s(\cdot; d) \frac{\partial}{\partial \nu} u^i(\cdot; -\hat{x}) - u^i(\cdot; -\hat{x}) \frac{\partial}{\partial \nu} u^s(\cdot; d) \right\} ds,$$

and interchanging the roles of  $\hat{x}$  and  $d$ ,

$$4\pi u_\infty(-d; -\hat{x}) = \int_{\partial D} \left\{ u^s(\cdot; -\hat{x}) \frac{\partial}{\partial \nu} u^i(\cdot; d) - u^i(\cdot; d) \frac{\partial}{\partial \nu} u^s(\cdot; -\hat{x}) \right\} ds.$$

We now subtract the last equation from the sum of the three preceding equations to obtain

$$4\pi \{ u_\infty(\hat{x}; d) - u_\infty(-d; -\hat{x}) \} = \int_{\partial D} \left\{ u(\cdot; d) \frac{\partial}{\partial \nu} u(\cdot; -\hat{x}) - u(\cdot; -\hat{x}) \frac{\partial}{\partial \nu} u(\cdot; d) \right\} ds.$$

**Eq. 3-42** follows by using the boundary condition

$$u(\cdot; d) = u(\cdot; -\hat{x}) = 0 \quad \text{on } \partial D.$$

We next review some properties of the Singular Value Decomposition of the response matrix [25, 26]. First, we review the concept singular value decomposition. Any complex matrix  $P$  can be written as  $P = U\Sigma V^H$ , where  $U$  and  $V$  are unitary, and

$$UU^H = I, \quad VV^H = I,$$

$$\Sigma = \begin{bmatrix} \text{diag}(\sigma_i) & 0 \\ 0 & 0 \end{bmatrix}.$$

Depending on the target size compared with the array resolution, the singular value decomposition of the response matrix can have the following three patterns.

For point targets with sizes much smaller than the array resolution, the number of significant singular values equals to the number of targets. In this case, the response matrix only contains location information. It is unrealistic to expect to recover shape information.

For small targets whose sizes are smaller than, but comparable to the array resolution, the pattern of singular values becomes more complicated [41]. The response matrix contains location and some size information.

For extended targets whose sizes are larger than the array resolution, the response matrix contains both location and geometry information of the target. It is no longer clear in the singular value plot how many singular values correspond to one target. In [25], a direct imaging algorithm is developed for extended target. The key idea in the imaging algorithm is to determine the illumination vector based on a physical factorization of the scattered field and the signal space as well as its dimension using resolution analysis.

We consider both near field and far field data. Therefore, the illumination vector should take the form in [25] and [26]. Here, we outline the procedure for far field data.

For near field it is similar. We consider sound-soft targets. For simplicity, we assume here that the outgoing directions we measure are the same as the incoming directions,  $\hat{\theta}_1, \dots, \hat{\theta}_n$ . The scattered far field is then [1]

$$u_\infty(\hat{x}) = -\frac{e^{i\pi/4}}{\sqrt{8\pi |k|}} \int_{\partial\Omega} \frac{\partial u}{\partial \nu}(y) e^{-ik\hat{x}\cdot y} ds(y), \quad \text{Eq. 3-43}$$

where  $\partial\Omega$  is the boundary of the targets,  $\hat{x}$  is a unit vector that defines the far field direction,  $u$  is the total field, and  $\nu$  is the outer normal direction on the boundary of the targets. In our setup, the element of the response matrix  $p_{ij}$  corresponds to the far field pattern of the scattered field in the  $j^{\text{th}}$  direction due to an incident wave coming from the  $i^{\text{th}}$  direction:

$$P_{ij} = u_\infty(\hat{\theta}_j; \hat{\theta}_i) = -\frac{e^{i\pi/4}}{\sqrt{8\pi |k|}} \int_{\partial\Omega} \frac{\partial u}{\partial \nu}(y; \hat{\theta}_i) e^{-ik\hat{\theta}_j \cdot y} ds(y), \quad \text{Eq. 3-44}$$

where the total field is due to incident plane wave coming from the direction  $\hat{\theta}_i$ . In matrix form

$$P = -\frac{e^{i\pi/4}}{\sqrt{8\pi |k|}} \int_{\partial\Omega} \frac{\partial \vec{u}}{\partial \nu} \hat{\mathbf{g}}^H(y) ds(y), \quad \text{Eq. 3-45}$$

where

$$\hat{\mathbf{g}}(y) = [e^{ik\hat{\theta}_1 \cdot y}, \dots, e^{ik\hat{\theta}_n \cdot y}]^T, \quad \text{Eq. 3-46}$$

and  $\vec{u}$  is the vector of total fields corresponding to the incident plane waves from  $\hat{\theta}_1, \dots, \hat{\theta}_n$ . Eq. 3-24 gives a physical factorization of the scattered field into known and unknown parts. The far field pattern is a superposition of the far field patterns of point sources located on the boundary of the target; however, we do not know the weight function which depends on the total field. In other words, the scattering at the target boundary acts as sources for the scattered field. In this far field setup, it is natural to use

$\hat{\mathbf{g}}(y)$  as the illumination vector. The signal space of the response matrix should be well approximated by the span of the illumination vectors  $\hat{\mathbf{g}}(y)$  with  $y$  on the well-illuminated part of the boundary of the targets.

The next step is to determine the signal space, which is spanned by appropriate singular vectors of the response matrix. It has been shown in [25] (for near field data) and [26] (for far field data) that by using a resolution analysis based thresholding, we could determine a threshold  $r$  and use the first  $r$  singular vectors to image the shape of the targets.

Let  $\mathbf{g}^0(\mathbf{x}) = [\mathbf{G}^0(\xi_1, \mathbf{x}), \dots, \mathbf{G}^0(\xi_N, \mathbf{x})]^T$  be the near field illumination vector. It is a collection of homogeneous Green's functions from the transducers to a search point  $\mathbf{x}$ . For the far field, the illumination vector is

$$\hat{\mathbf{g}}(x) = [e^{ik\hat{\theta}_1 \cdot x}, \dots, e^{ik\hat{\theta}_N \cdot x}]^T,$$

where  $\hat{\theta}_i$  are incident plane wave directions.

Let  $\vec{u}_1, \vec{u}_2, \dots, \vec{u}_M$  be the set of singular vectors that span the signal space  $V^S$ . The imaging function for MUSIC for near field is defined by

$$I(x) = \frac{1}{\|\vec{g}^0(x)\|^2 - \|P_{V^S} \vec{g}^0(x)\|^2} = \frac{1}{\|\vec{g}^0(x)\|^2 - \sum_{k=1}^M |\vec{g}^0(x) \cdot \vec{u}_k|^2}. \quad \text{Eq. 3-47}$$

For far field, we just use the far field illumination vector.

In [25], resolution analysis is discussed to estimate the dimension of the signal space  $M$ . We use a kite shape example below to demonstrate what would go wrong if we have an underestimate or an overestimate for the dimensions of the signal space. In **Figure 3-2**, we could see with an underestimate of the signal space that the imaging function seems to be representing a collection of some point targets. With an

overestimate, the imaging function would provide a larger image than it should be and the shape is distorted. However, there is a safe zone of choices of acceptable estimated dimensions. For instance, in this example, using  $M$  from 18 to 36 seems to provide acceptable images.

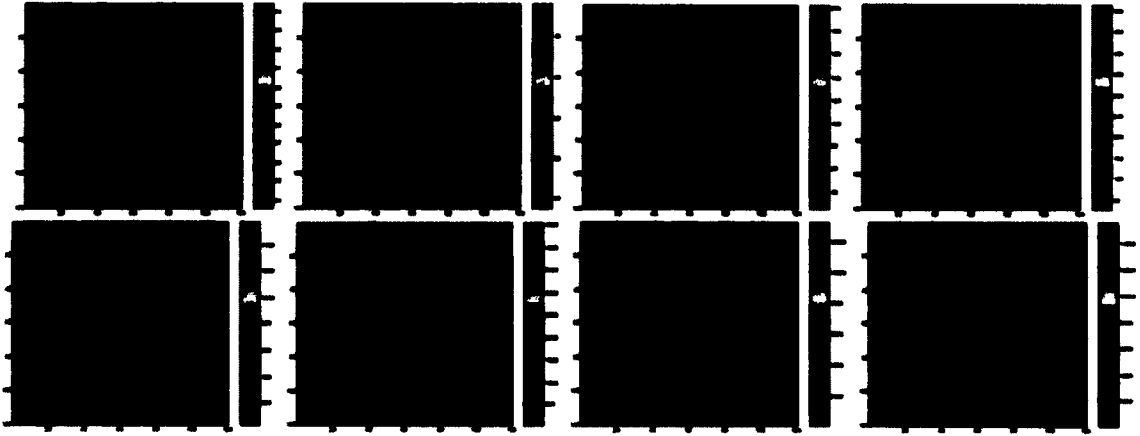


**Figure 3-2:** Imaging Results ( $M = 1, 5, 18, 24$  for Row 1 and  $M = 30, 36, 42, 48$  for Row 2). [25]

In this dissertation, we propose to use the singular values as the natural weight to get around the above thresholding procedure. The imaging function we use is

$$I_2(x) = (g^0(x))^H P \bar{g}^0(x) = (g^0(x))^H \left( \sum_{k=1}^N \sigma_k u_k v_k^H \right) \bar{g}^0(x). \quad \text{Eq. 3-48}$$

This imaging function is motivated by the following idea: From the reciprocity relation [1], we know the response matrix is complex symmetric:  $P = P^T$ . We have the following special singular value decomposition  $P = U \Sigma U^T$ . In other words,  $U = \bar{V}$ . The

essential part of the MUSIC algorithm is

$$I_0(x) = \sum_{k=1}^M |\vec{g}^{\hat{0}}(x) \cdot \vec{u}_k|^2. \quad \text{Eq. 3-49}$$

The idea of multi-tone imaging is to remove the absolute value to keep the phase information for  $U = \bar{V}$  case:

$$I_1(x) = \sum_{k=1}^M (\vec{g}^{\hat{0}}(x) \cdot \vec{u}_k)^2. \quad \text{Eq. 3-50}$$

The general form of multi-tone imaging function takes the form

$$\tilde{I}_1(x) = \sum_{k=1}^M (\vec{g}^{\hat{0}}(x) \cdot \vec{u}_k)(\vec{g}^{\hat{0}} \cdot \vec{v}_k). \quad \text{Eq. 3-51}$$

Now if we use singular values as natural weight, we could sum from 1 to N instead and get Eq. 3-48. The phase information is kept since no absolute value is taken (unlike the MUSIC algorithm) and the singular values serve as natural weight so that resolution analysis is not necessary.

One major drawback of the MUSIC-type algorithms [25, 26] is that such algorithms are projection algorithms that remove the phase information. It is not meaningful to combine multiple frequency projection results. For full aperture data, the MUSIC-type algorithms work so well that the drawback is disguised. However, for synthetic aperture data, which is more realistic in some applications, the results from the MUSIC algorithms degenerate. It is crucial to take advantage of the phase coherence to overcome the challenge of lack of data [27]. We will show in Section 4.2 that numerical the results using low frequency data are more robust but less accurate; numerical results using high frequency data are more accurate but less robust. By combining multiple frequency results while keeping the phase information, we could generate accurate and

robust results. Furthermore, efficiency is guaranteed since there is no need for iteration. The evaluations at different grid points are also independent, making it easy to be parallelized.

Singular Value Decomposition (SVD) is a very important process in the direct imaging method. We briefly describe two important theorems, Mirsky's Theorem and G.W. Stewart's Theorem, as they are significant previous work to estimate the perturbation of singular values.

For the  $m$ -by- $n$  ( $m \leq n$ ) matrix  $A$ , there exists no more than  $m$  non-zero singular values  $\sigma_i(A)$ . If we define  $\lambda_1 \geq \lambda_2 \geq \dots \geq \lambda_m$  as matrix  $A$ 's ordered eigenvalues, we simply can have

$$\sigma_i(A) = \sqrt{\lambda_i(A^T A)}, \quad \text{where } i = 1, 2, 3, \dots, m. \quad \text{Eq. 3-52}$$

In Mirsky's Theorem [6, 30, 37, 38], the perturbation of singular values are estimated by a unitarily invariant norm of the matrix perturbation. In particular, for 2-norm we have

$$\text{Max}_i |\sigma_i(A + E) - \sigma_i(A)| \leq \|E\|_2, \quad \text{for } i = 1, 2, 3, \dots, m. \quad \text{Eq. 3-53}$$

Mirsky's Theorem gives us an estimate for all singular values. However, the signal space in a direct imaging method is only spanned by the first few singular values. The estimate from Mirsky's Theorem is not sharp enough for its need in the direct image method.

G.W. Stewart's Theorem [13, 21] can be described as follows:

Let  $F$  be a matrix valued function for matrix  $A$ . For another given matrix  $E$ , which is presumed to be small, we are trying to approximate  $F(A + E)$  by bounding the norm of  $(F(A + E) - F(A))$  in terms of the norm of  $E$ .

This theorem has two basic ideas. The first one is to assume that  $F$  is differentiable at  $A$  with a derivative function  $F_A$ . Then we have

$$F(A + E) = F(A) + F_A(E) + o(\|E\|). \quad \text{Eq. 3-54}$$

In this case, for sufficiently small  $E$ ,  $F_A(E)$  is the required approximation and the problem can be reduced to finding tractable expressions for  $F_A(E)$ . The second idea is to use the perturbation size as an overestimated upper bound.

However, from these two basic ideas, we acknowledge that the Stewart's Theorem is based on the assumption of small perturbation. In the case where noise has large perturbation, the basic assumption of the theorem cannot be satisfied.

Since Mirsky's Theorem and Stewart's Theorem could not completely solve our problem, we need new estimates for singular values. Based on a fact that the 2-norm of a matrix is exactly the largest singular value of the matrix, we use matrix norms to estimate the singular value. The 1-norm and  $\infty$ -norm can be computed as

$$\|A\|_1 = \max_{1 \leq j \leq n} \sum_{i=1}^m |a_{ij}|, \quad \text{Eq. 3-55}$$

$$\|A\|_\infty = \max_{1 \leq i \leq n} \sum_{j=1}^m |a_{ij}|. \quad \text{Eq. 3-56}$$

From the formulas, the summation corresponds to averaging. The "max" gives a bias. Following the Central Limit Theorem given certain conditions, the mean of a sufficiently large number of independent random variables, each with finite mean and variance will be approximately normally distributed. Therefore, the 1-norm and  $\infty$ -norm have a "normal distribution with bias".

The first singular value  $\sigma_1$  equals the matrix 2-norm  $\|A\|_2$ . For 2-norm, we have the norm equivalence:

$$\|A\|_\infty/\sqrt{n} \leq \|A\|_2 \leq \sqrt{m}\|A\|_\infty, \quad \text{Eq. 3-57}$$

$$\|A\|_1/\sqrt{m} \leq \|A\|_2 \leq \sqrt{n}\|A\|_1. \quad \text{Eq. 3-58}$$

Thus, the lower and upper bounds for 2-norm, when perturbed, have normal distribution with bias. So we expect 2-norm to have normal distribution with bias, and tend to be larger as well. If this property can be proven, we can successfully estimate the singular value. Unfortunately, the property is not a deterministic property: for example, we could perturb all elements by 100% to be zeros and the singular values have large perturbation. This means the robustness of singular value holds in a probability sense: it is highly likely that the singular value is robust. Such property is extremely difficult to prove rigorously, or even state rigorously. Therefore, we rely on numerical test instead.

**Figure 3-3** shows 10,000 realizations for the first singular value of perturbed matrices with 100% noise. In most of the realizations, the singular value is only perturbed by less than 15%. The **Figure 3-4** shows how many realizations fall into each interval. This figure clearly exhibits the normal distribution. The first singular value before a 100% perturbation is 4.1726. The average of 10,000 realizations of perturbed singular values is 4.9486. This clearly demonstrates a bias (tends to be larger), as explained earlier.

From the above discussion, we know the singular values are robust with respect to noise. That is the reason why our direct imaging algorithm can handle large measurement noise. This will be illustrated in Section 4.2.

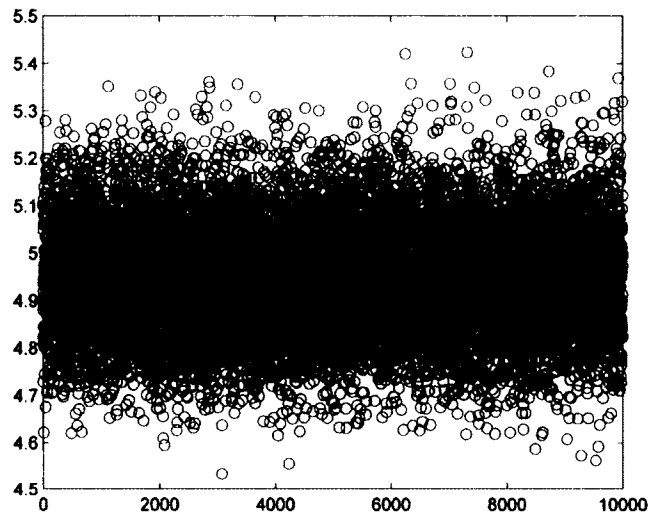


**Figure 3-3:** Singular Value Perturbation for 10,000 Realizations.

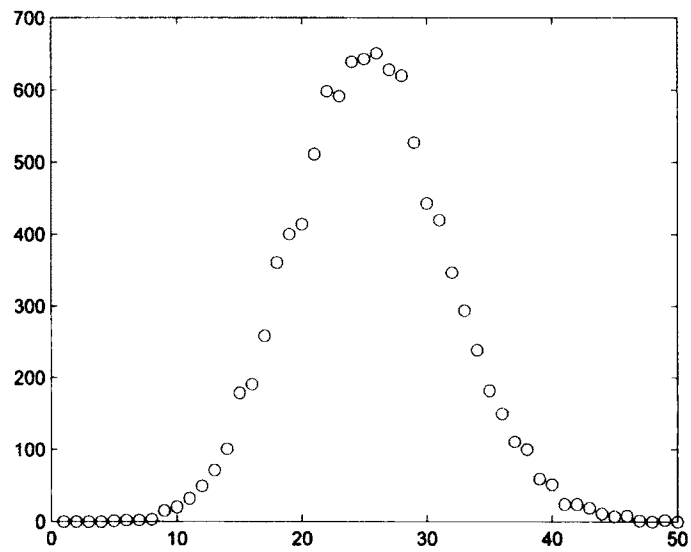


**Figure 3-4:** Singular Value Count Falling into Consecutive Intervals with Equal Spacing.

## CHAPTER 4

### RESULTS

In this chapter, we present some numerical examples to demonstrate the effectiveness of our method.

#### 4.1 The Forward Problem

We first present results for a smooth target, reproducing the work from [1]. **Figure 4-1** shows the geometry of a “kite” with grid points on its boundary. **Table 4-1** shows the error of  $\max(\max(|p_n - p_{128}|))$  where  $n = 16, 32, 64$ , where  $2n$  is the number of points used on the boundary of the kite shape. Exponential convergence is exhibited since the number of correct digits doubles when  $n$  doubles. Note that for the fine grid  $n = 64$  compared with  $n = 128$ , the error reaches machine precision. The result is consistent with [1]. For most applications,  $2^{\text{nd}}$  order convergence is already a desired result for a numerical method. Exponential convergence is much faster than  $2^{\text{nd}}$  order convergence. The equation for the kite-shaped is

$$x(t) = (\cos t + 0.65 \cos 2t - 0.65, 1.5 \sin t), \quad 0 \leq t \leq 2\pi.$$

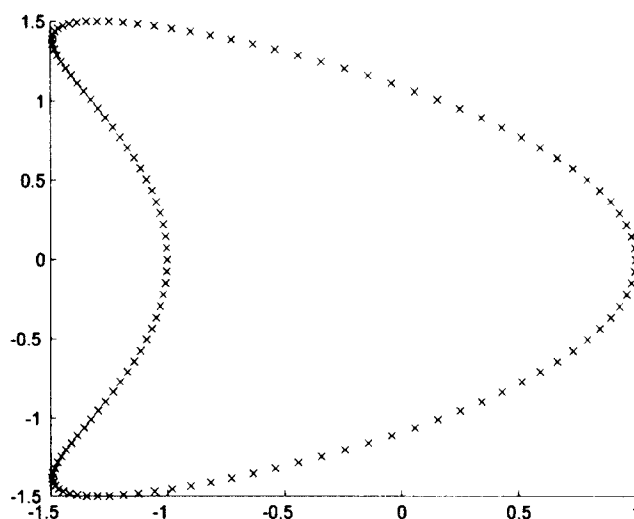


**Figure 4-1:** The Mesh for “Kite” Shape.

**Table 4-1:** Error of “Kite” with Grid Number  $n = 16, 32, 64$ .

Grid Number	$n = 16$	$n = 32$	$n = 64$
Error of Max	2.1299e-05	9.3405e-11	1.8595e-14

Next, we present an example with three corners. In [1], an example with one corner was presented. However, if we follow the procedure to treat three corners, a large condition number is observed. By using the method in Section 3.1, we reduced the condition number. **Figure 4-2** shows the geometry of “three corners” with grid points on its boundary. Note that we used graded mesh. About half of the grid points are near the corners. **Table 4-5** shows the error of  $\max(\max(|p_n - p_{128}|))$  for  $n = 16, 32, 64$ , where  $n$

is the number of points on one of the three arcs. **Table 4-2** to **Table 4-4** show the errors for eight incident directions and eight scattering directions.

Due to the corner singularities, we no longer have exponential convergence. Still, high order convergence is exhibited. The equations for each arc of the three-corners are:

$$x = \cos\left(\frac{\theta}{2} + \frac{\pi}{6}\right),$$

$$y = \sin\left(\frac{\theta}{2} + \frac{\pi}{6}\right),$$

$$x = \cos\left(\frac{\theta}{2} + \frac{\pi}{2}\right) + \frac{\sqrt{3}}{2},$$

$$y = \sin\left(\frac{\theta}{2} + \frac{\pi}{2}\right) + \frac{1}{2},$$

$$x = \cos\left(\frac{\theta}{2} + \frac{5\pi}{6}\right),$$

$$y = \sin\left(\frac{\theta}{2} + \frac{5\pi}{6}\right) + 1.$$

**Table 4-2**, **Table 4-3**, **Table 4-4** and **Table 4-5** list the response matrix error of “Three Corners”.

**Table 4-2:** Response Matrix Error ( $n = 16$ ) ( $\times 10^{-3}$ ).

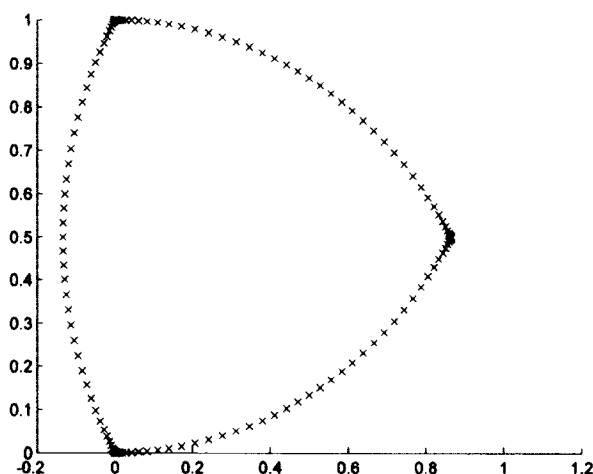
0.5327	0.6086	0.5931	0.4569	0.4684	0.4241	0.5487	0.7204
0.7073	0.6458	0.5717	0.2678	0.4976	0.4501	0.2841	0.5558
0.4694	0.4532	0.4189	0.4174	0.3970	0.0538	0.3638	0.3704
0.4102	0.1147	0.3591	0.7374	0.3591	0.1147	0.4102	0.4539
0.3638	0.0538	0.3970	0.4174	0.4189	0.4532	0.4695	0.3704
0.2841	0.4503	0.4976	0.2678	0.5717	0.6458	0.7073	0.5558
0.5487	0.4241	0.4684	0.4569	0.5931	0.6086	0.5327	0.5327
0.6897	0.3566	0.1882	0.3091	0.1882	0.3566	0.6897	0.9971

**Table 4-3:** Response Matrix Error ( $n = 32$ ) ( $\times 10^{-4}$ ).

0.5327	0.6086	0.5931	0.4569	0.4684	0.4241	0.5487	0.7204
0.7073	0.6458	0.5717	0.2678	0.4976	0.4501	0.2841	0.5558
0.4694	0.4532	0.4189	0.4174	0.3970	0.0538	0.3638	0.3704
0.4102	0.1147	0.3591	0.7374	0.3591	0.1147	0.4102	0.4539
0.3638	0.0538	0.3970	0.4174	0.4189	0.4532	0.4695	0.3704
0.2841	0.4503	0.4976	0.2678	0.5717	0.6458	0.7073	0.5558
0.5487	0.4241	0.4684	0.4569	0.5931	0.6086	0.5327	0.5327
0.6897	0.3566	0.1882	0.3091	0.1882	0.3566	0.6897	0.9971

**Table 4-4:** Response Matrix Error ( $n = 64$ ) ( $\times 10^{-6}$ ).

0.2326	0.2642	0.2802	0.2058	0.2040	0.2055	0.2402	0.2836
0.3195	0.3006	0.2062	0.1300	0.2371	0.2022	0.1140	0.2707
0.2377	0.2309	0.1334	0.2532	0.1806	0.0391	0.2002	0.1972
0.1912	0.0361	0.1903	0.3373	0.1922	0.0316	0.2022	0.2062
0.2002	0.0300	0.1806	0.2574	0.1354	0.2220	0.2297	0.1910
0.1131	0.2022	0.2441	0.1393	0.2062	0.3007	0.3231	0.2622
0.2402	0.2138	0.2040	0.2025	0.2804	0.2697	0.2376	0.2780
0.2930	0.1844	0.1140	0.1020	0.1063	0.1860	0.2907	0.3517

**Figure 4-2:** “Three Corners” with Graded Mesh.

**Table 4-5:** Error of “Corners” with Grid Number ( $n = 16, 32, 64$ ).

Grid Number	$n=16$	$n=32$	$n=64$
Error of Max	9.9706e-04	2.2081e-05	3.517e-07

Next, we present a more complicated example with the geometry of a butterfly with many corners. The equations for each arc of the butterfly are:

$$y = -\frac{1}{2}(x - 1)^2 + 1,$$

$$x = -\frac{1}{2}(y - 1)^2 + 1,$$

$$x = -\frac{3}{8}\left(y + \frac{2}{3}\right)^2 + \frac{2}{3},$$

$$y = \frac{3}{4}\left(x - \frac{2}{3}\right)^2 - \frac{2}{3},$$

$$y = \frac{3}{4}\left(x + \frac{2}{3}\right)^2 - \frac{2}{3},$$

$$x = \frac{3}{8}\left(y + \frac{2}{3}\right)^2 - \frac{2}{3},$$

$$x = \frac{1}{2}(y - 1)^2 - 1,$$

$$y = -\frac{1}{2}(x + 1)^2 + 1.$$

We first denote  $n$  to be the number of points on the shortest arc. By using the ratio between arc lengths, we could assign the number of points on each arc. Then we have an equal partition for a parameter with ranges between  $[0, 2\pi]$ . Finally, we map the points to the graded mesh in Section 3.1. **Figure 4-3** shows the butterfly geometry with graded mesh. **Table 4-8** shows the error of  $\max(\max(|p_n - p_{64}|))$  for  $n = 16, 32$ , where  $n$  is the number of points on the shortest arc. Again, high order convergence is exhibited.

The response matrices of “Butterfly” are shown in **Table 4-6** to **Table 4-8**:

**Table 4-6:** Response Matrix Error ( $k = 7, n = 16$ ).

0.0006	0.0005	0.0007	0.0007	0.0002	0.0003	0.0005	0.0005
0.0016	0.0010	0.0013	0.0016	0.0005	0.0006	0.0015	0.0014
0.0015	0.0016	0.0021	0.0016	0.0003	0.0011	0.0020	0.0011
0.0013	0.0006	0.0012	0.0012	0.0005	0.0006	0.0013	0.0010
0.0003	0.0003	0.0005	0.0004	0.0003	0.0005	0.0004	0.0003
0.0005	0.0002	0.0006	0.0004	0.0003	0.0005	0.0004	0.0003
0.0006	0.0005	0.0007	0.0005	0.0002	0.0004	0.0006	0.0004
0.0002	0.0003	0.0005	0.0001	0.0000	0.0002	0.0004	0.0001

**Table 4-7:** Response Matrix Error ( $k = 7, n = 32$ ) ( $\times 10^{-4}$ ).

0.2611	0.2138	0.3008	0.2723	0.0696	0.1436	0.2726	0.2005
0.6779	0.4829	0.7068	0.6794	0.1895	0.3368	0.7190	0.5358
0.8289	0.7203	0.9910	0.8372	0.1892	0.4822	0.9633	0.6278
0.5266	0.3520	0.5518	0.5200	0.1469	0.2628	0.5633	0.4061
0.1456	0.1024	0.1961	0.1651	0.0438	0.1137	0.1925	0.1248
0.1724	0.1194	0.1880	0.1507	0.0668	0.1285	0.1507	0.1229
0.2108	0.1752	0.2126	0.1853	0.0714	0.1412	0.1977	0.1481
0.1052	0.1035	0.1600	0.0985	0.0223	0.0739	0.1561	0.0625

**Table 4-8:** Error of “Butterfly” with  $n = 16, 32$ .

Grid Number	$n = 16$	$n = 32$
Error of Max	0.0023	1.060e-04

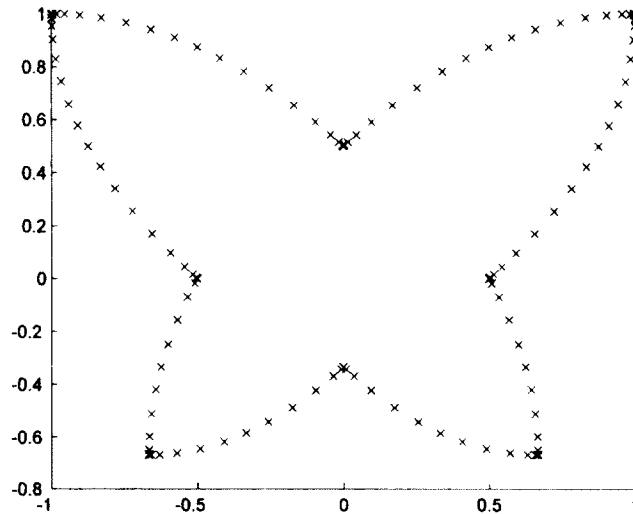


**Figure 4-3:** “Butterfly” with Graded Mesh.

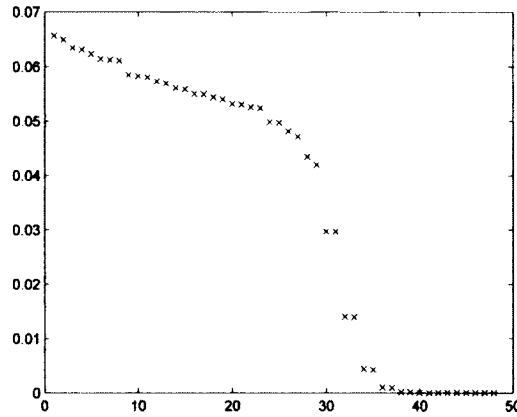
Now we demonstrate the relation among the response matrices for near field and far field data. We compare the following four cases.

1. Plane incident wave, far field data
2. Plane incident wave, near field data with  $r = 5$
3. Point source with  $r = 5$ , far field data
4. Point source with  $r = 5$ , near field data with  $r = 5$

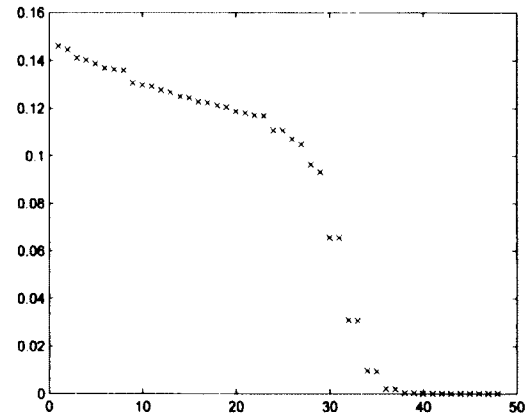
Here,  $r$  means the radius of the circle on which the transducers are placed.

In Section 3.1, we derived the relation among the above matrices. Now we use a numerical example to verify the results. We choose the butterfly shape as the obstacle.

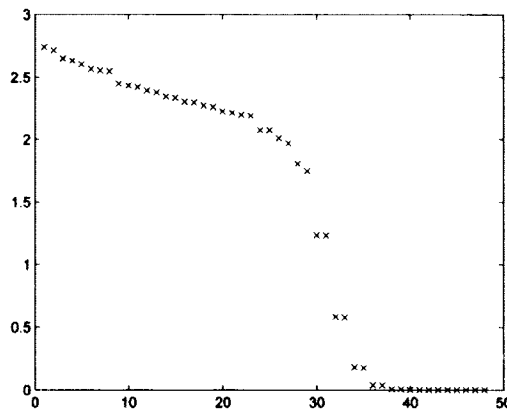
**Figure 4-4** contain the plots for the singular values of the four response matrices.



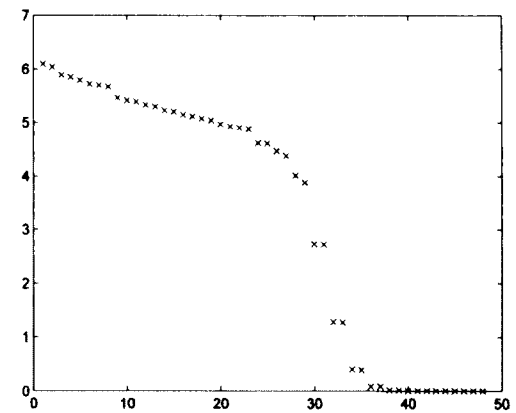
Plane Incident Wave, Far Field Data



Plane Incident Wave, Near Field Data



Point Source, Far Field Data



Point Source, Near Field Data

**Figure 4-4:** Singular Value Plots for Near and Far Field Response Matrices.

They clearly share the same pattern with different scales. Next, we justify the relations **Eq. 3-39-Eq. 3-41**, numerically. We use the butterfly shape. We find that

$$\sigma_{1,1} = 0.0656,$$

$$\frac{1}{\sqrt{r}}\sigma_{1,2} = 0.0653,$$

$$\sigma_{1,3} = 2.7387,$$

$$\frac{1}{\sqrt{r}}\sigma_{1,4} = 2.7250,$$

$$\sigma_{1,2} = 0.1460,$$

$$\frac{1}{\sqrt{8\pi k}}\sigma_{1,3} = 0.1460,$$

$$\max(\max(|p_2 - \beta p_3^T|)) = 7.0647 \times 10^{-5}.$$

Note that  $\sigma_{1,1} > \frac{1}{\sqrt{r}}\sigma_{1,2}$ ,  $\sigma_{i,3} > \frac{1}{\sqrt{r}}\sigma_{1,4}$ . The reason is that with a perturbation of matrix elements without bias, the singular values are more likely to get larger.

Now we present numerical results to justify our claim in Section 3.1 for the condition number. For the shape with three corners with  $n = 32$ , the condition number for the two methods are 14 and 47,135. For the butterfly shape, with  $n = 32$ , they are 90 and 6,353. Clearly, by modifying the method in [10], the condition number is significantly reduced. This justifies our claim that the method in [1] for one corner needs to be slightly modified for the case with multiple corners.

## 4.2 The Inverse Problem

We now use some numerical examples to demonstrate the accuracy, efficiency and robustness of our method in Section 3.2 for solving the inverse obstacle problem.

Our first example is the butterfly shape. The response matrix is generated by the forward solver in Section 3.1.

In the previous discussion, we found the similarity among the response matrices for four cases: point source or plane wave incident, near field or far field data. Therefore, we expect the inverse problem solver to produce similar results for the four cases. The only place we need to make change is the form of illumination vector for the source and the receiver. **Figure 4-5** shows the low frequency, middle frequency, high frequency and

multiple frequency results for a butterfly shape target with plane incident wave and far field data.

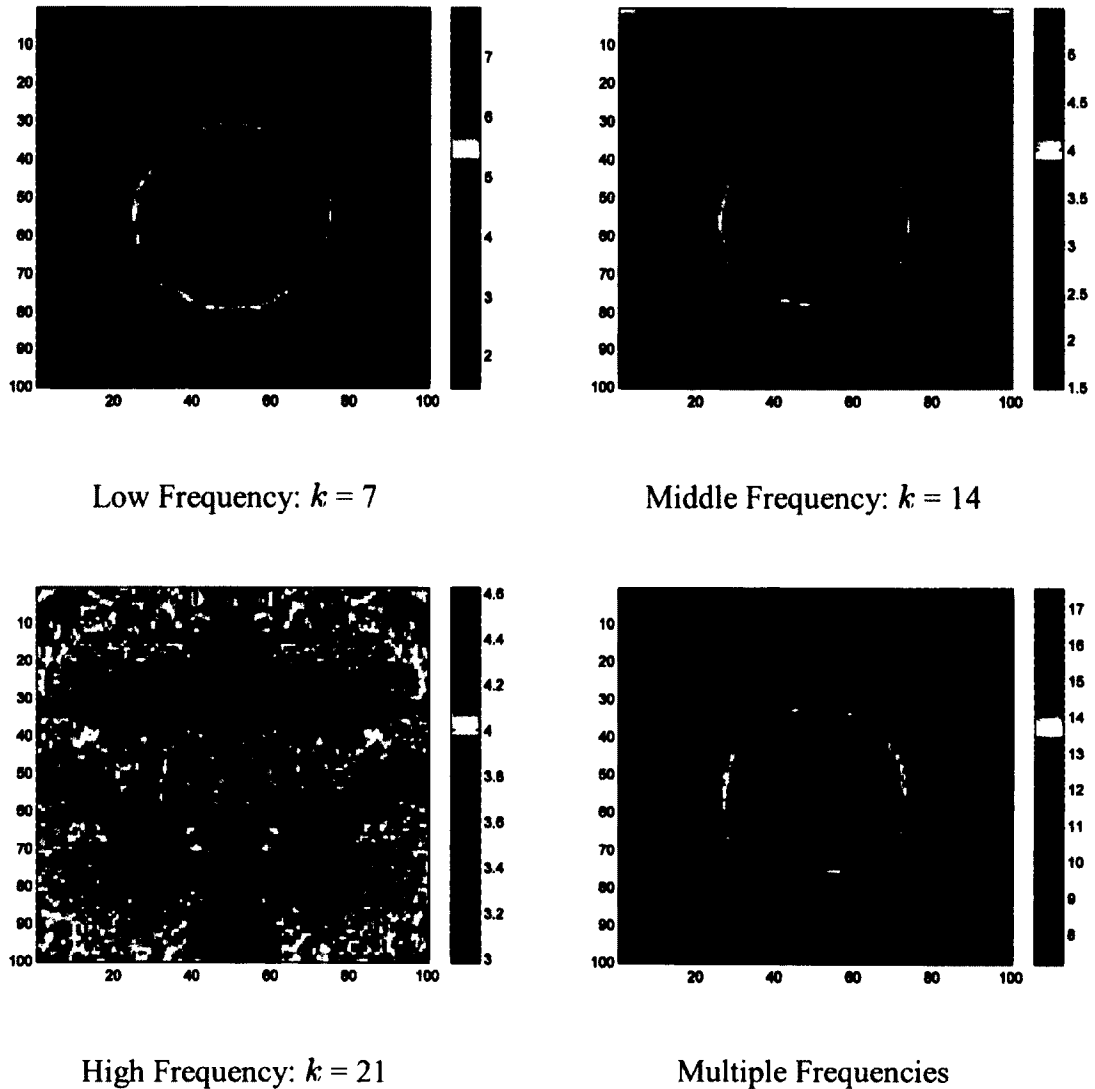


**Figure 4-5:** “Butterfly” with Plane Incident Wave, Far Field Data.

The low frequency result is robust but not accurate: the background clearly separates from the target. The target boundary is not sharp, however. The high frequency result is more accurate but less robust: the background has some artifacts. The target boundary is sharper. By combining multiple frequency data, the result is both accurate

and robust. We are able to overcome the challenges in inverse problems: the nonlinearity and ill-posedness. Also, note that the butterfly shape is not convex and multiple scattering between the concave edges makes imaging a difficult task. Still, our result is promising. **Figure 4-6** shows the low frequency, middle frequency, high frequency and multiple frequency results for a butterfly shape target with Plane incident wave, near field data with  $r = 5$ .

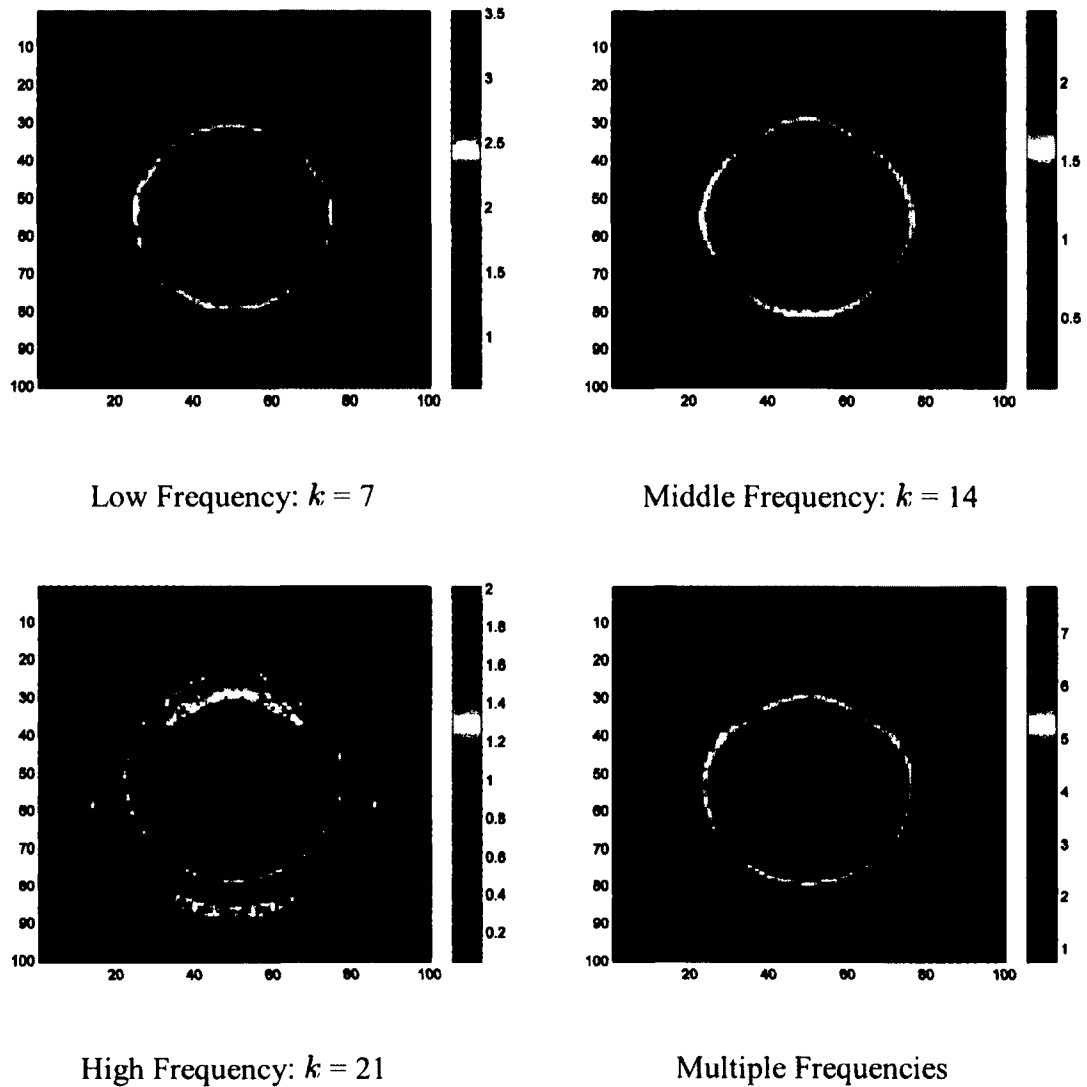


**Figure 4-6:** “Butterfly” Plane Incident Wave, near Field Data with  $r = 5$ .

Figure 4-7 shows the low frequency, middle frequency, high frequency and multiple frequency results for a butterfly shape target with point source with  $r = 5$ , far field data.

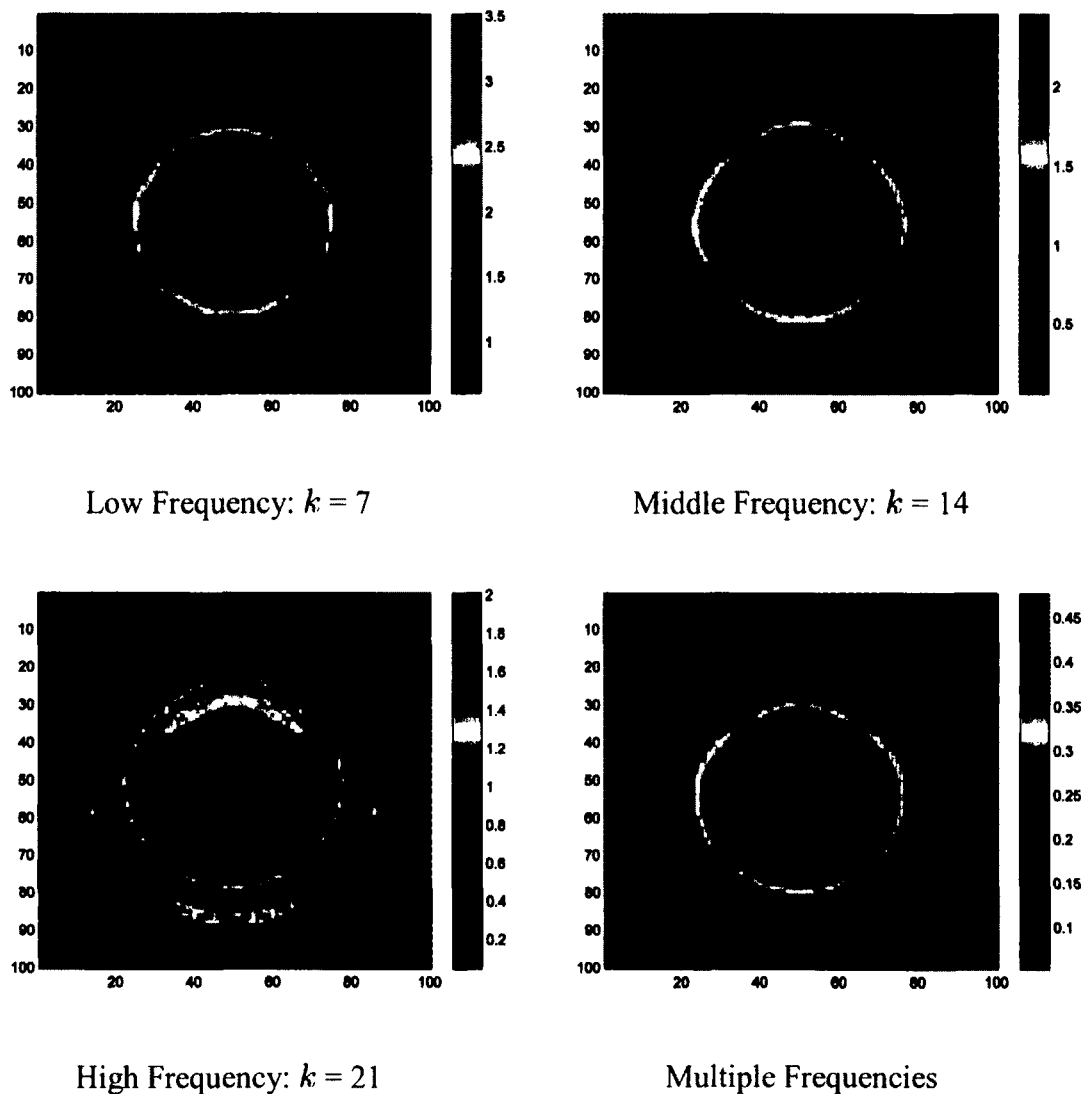
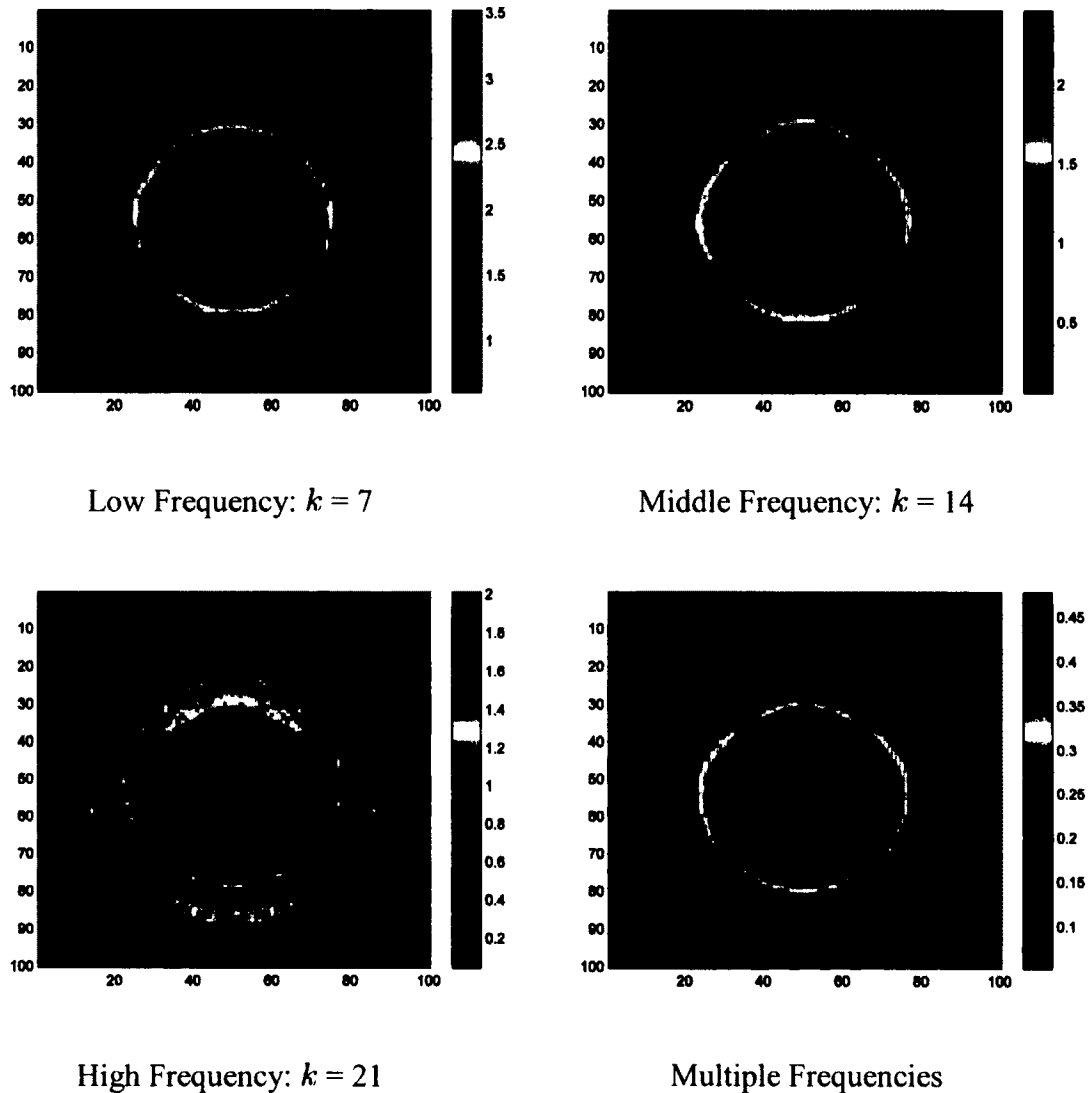


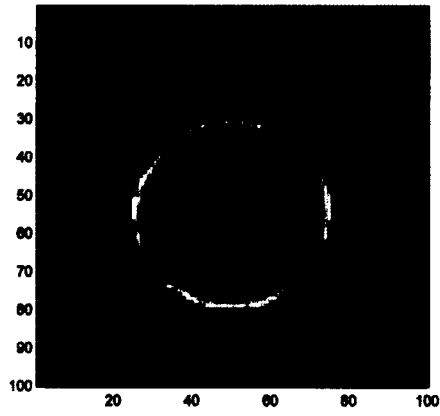
Figure 4-7: “Butterfly” Point Source with  $r = 5$ , Far Field Data.

Figure 4-8 shows the low frequency, middle frequency, high frequency and multiple frequency results for a butterfly shape target with point source with  $r = 5$ , near field data with  $r = 5$ .

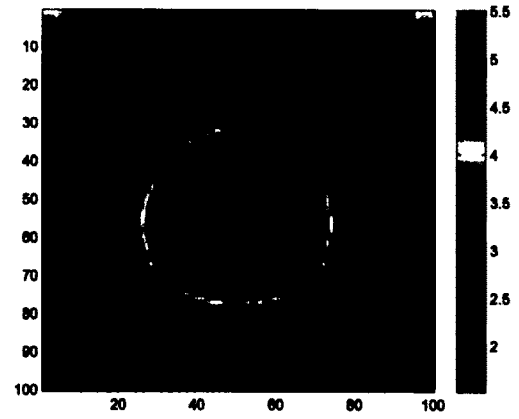


**Figure 4-8:** “Butterfly” Point Source with  $r = 5$ , near Field Data with  $r = 5$ .

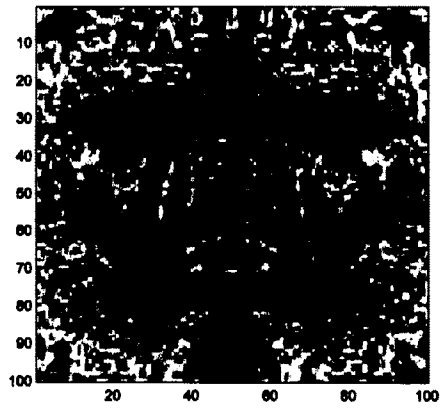
To demonstrate the robustness of our method, we add 20% noise to the response matrix. To be more precise, let  $P_{ij} = P_{ij}^r + iP_{ij}^i$  be one element of the response matrix, where  $P_{ij}^r, P_{ij}^i$  are real and imaginary parts. Let  $\widetilde{P}_{ij} = P_{ij}^r * a + iP_{ij}^i * b$  where  $a, b$  are random numbers uniformly distributed in  $[1 - 0.2, 1 + 0.2]$ , i. e. ,  $[0.8, 1.2]$ . **Figure 4-9** to **Figure 4-12** show the results after adding noise to the response matrices.



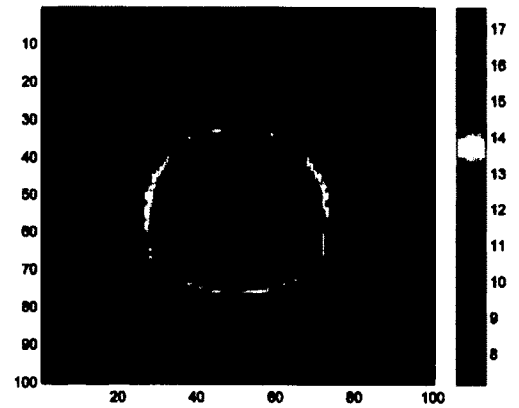
Low Frequency:  $k = 7$



Middle Frequency:  $k = 14$

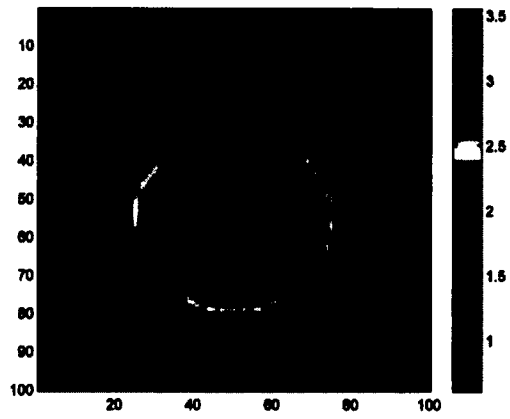


High Frequency:  $k = 21$

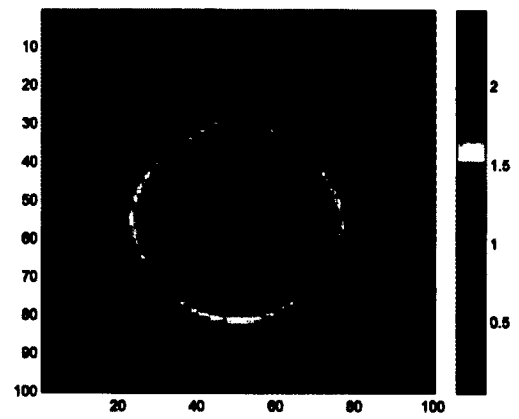


Multiple Frequencies

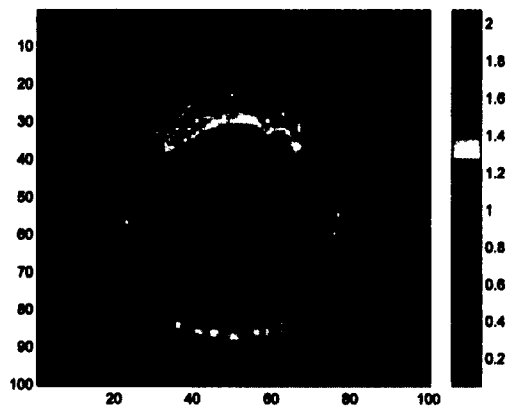
**Figure 4-9:** “Butterfly” with Plane Incident Wave, Far Field Data with Noise.



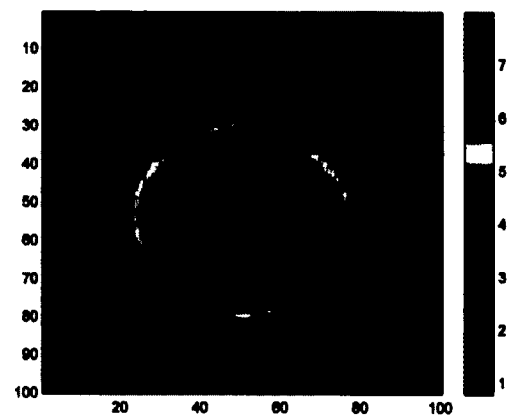
Low Frequency:  $k = 7$



Middle Frequency:  $k = 14$



High Frequency:  $k = 21$



Multiple Frequencies

**Figure 4-10:** “Butterfly” Plane Incident Wave, near Field Data with  $r = 5$  with Noise.

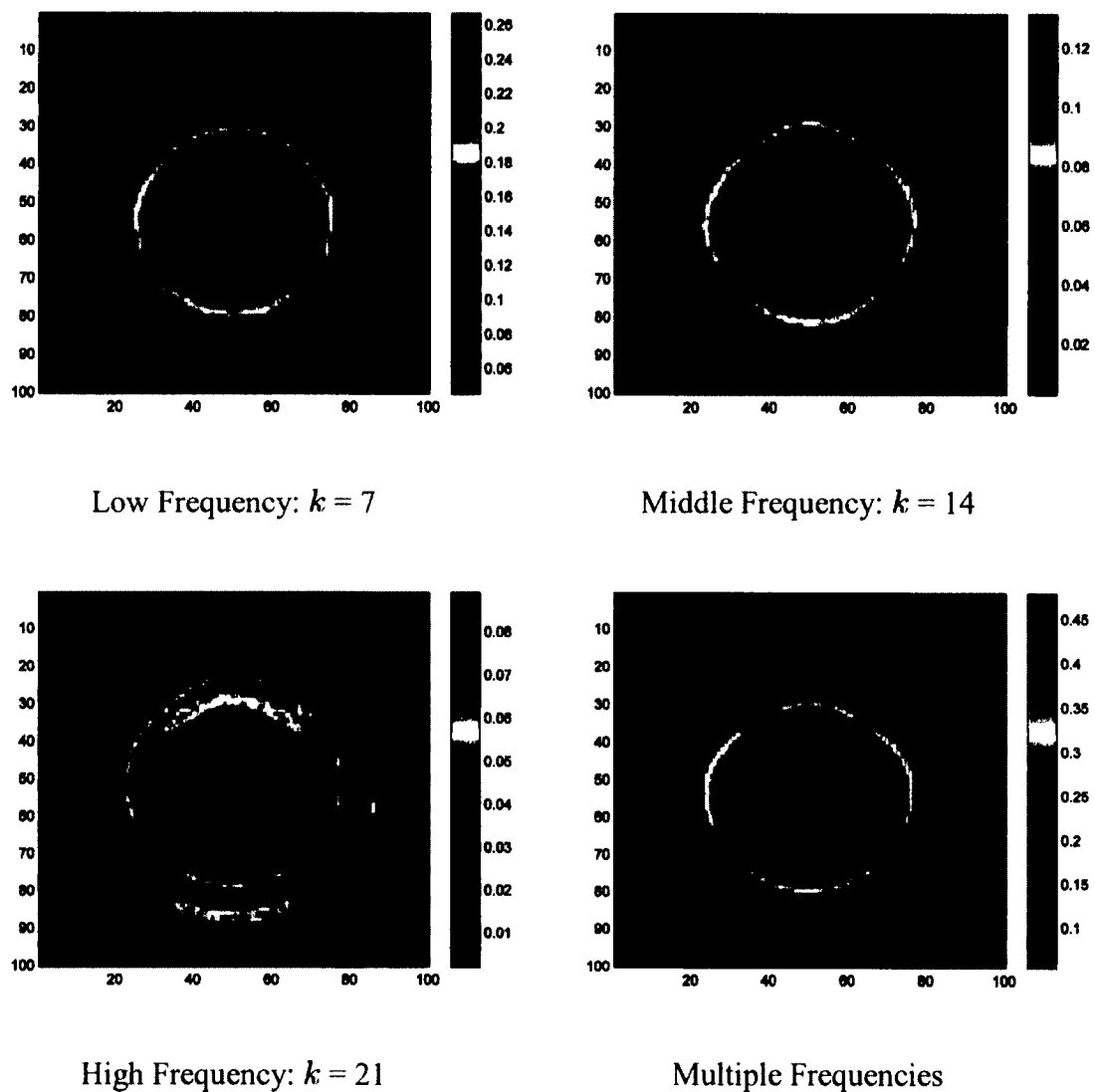
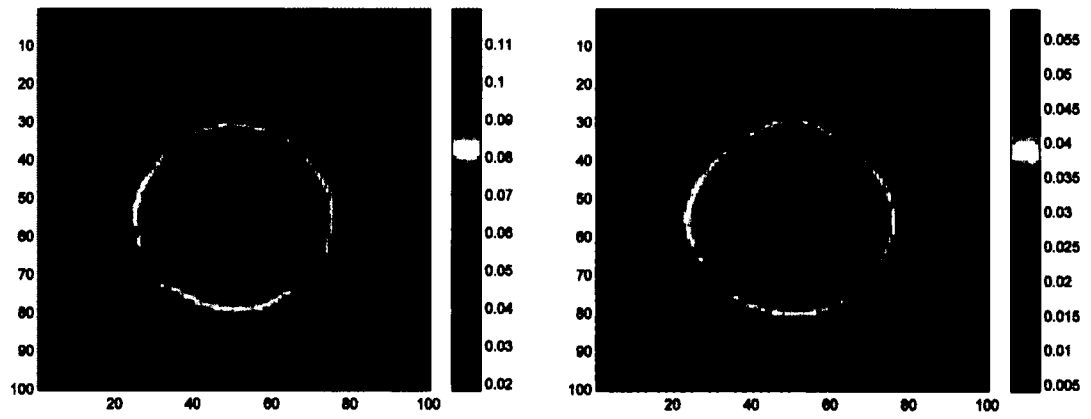
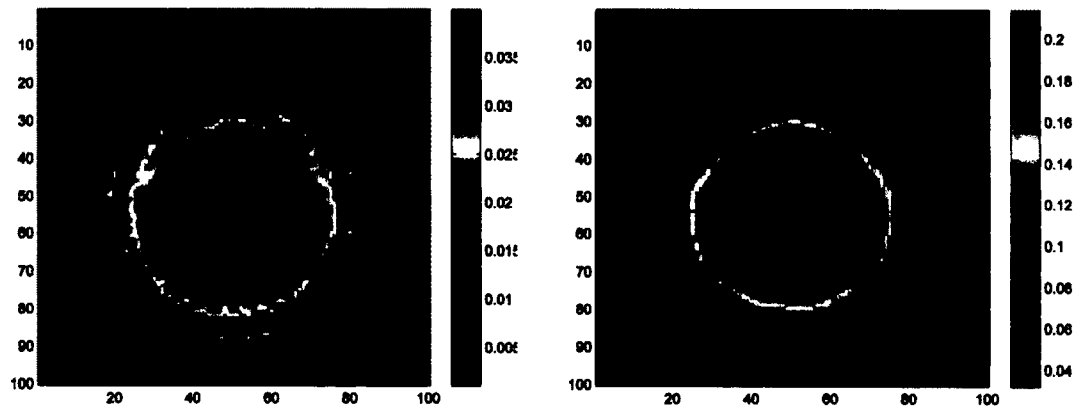


**Figure 4-11:** “Butterfly” Point Source with  $r = 5$ , Far Field Data with Noise.



Low Frequency:  $k = 7$

Middle Frequency:  $k = 14$



High Frequency:  $k = 21$

Multiple Frequencies

**Figure 4-12:** “Butterfly” Point Source with  $r = 5$ , near Field Data with  $r = 5$  with Noise.

We also presented another complicated example with the geometry of a “Paw” with many corners, see **Figure 4-13**. In this example, we only process low frequency, middle frequency, high frequency and multiple frequency results for a “Paw” shape target with plane incident wave and far field data. Notice that we use lower frequencies compared with the cases for “Butterfly” because the “Paw” is larger, corresponding to larger wavelength and thus lower frequency, for the same resolution.

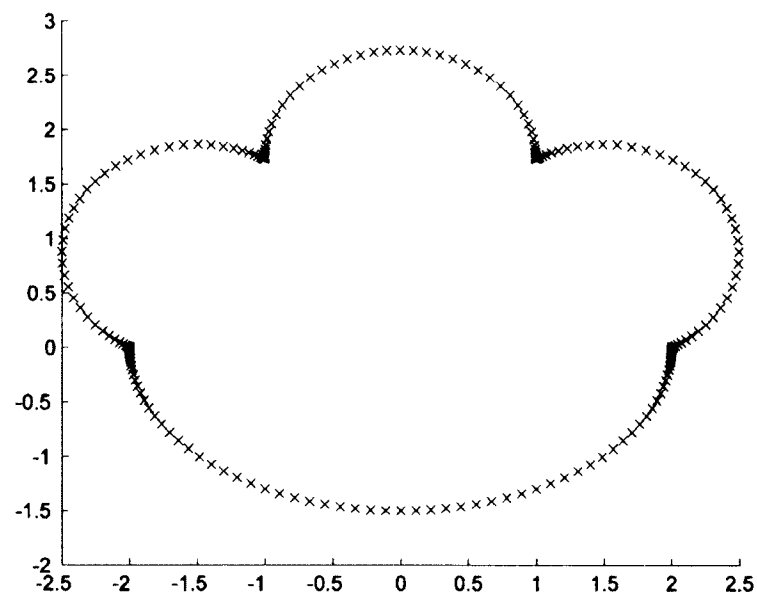


**Figure 4-13:** “Paw” with Graded Mesh.

The equations for each arc of the “Paw” are:

$$x = \frac{3}{2} + \cos \theta,$$

$$y = \frac{\sqrt{3}}{2} + \sin \theta,$$

$$x = \cos \theta,$$

$$y = \sqrt{3} + \sin \theta,$$

$$x = -\frac{3}{2} + \cos \theta,$$

$$y = \frac{\sqrt{3}}{2} + \sin \theta,$$

$$x = 2 \cos \theta,$$

$$y = \frac{3}{2} \sin \theta.$$

The response matrices error compared with fine grid  $n = 64$  of “Paw” are listed in Table 4-9 and Table 4-10. High order convergence is observed, though not as good as exponential convergence for the smooth target case.

**Table 4-9:** Response Matrix Error ( $k = 4, n = 16$ )

0.0184	0.0051	0.0042	0.0080	0.0129	0.0110	0.0111	0.0141
0.0079	0.0021	0.0065	0.0046	0.0045	0.0108	0.0019	0.0027
0.0005	0.0088	0.0281	0.0004	0.0040	0.0066	0.0093	0.0066
0.0049	0.0008	0.0060	0.0067	0.0143	0.0100	0.0069	0.0104
0.0126	0.0052	0.0011	0.0093	0.0186	0.0222	0.0117	0.0074
0.0107	0.0083	0.0030	0.0078	0.0226	0.0325	0.0185	0.0102
0.0087	0.0028	0.0079	0.0047	0.0150	0.0207	0.0034	0.0040
0.0081	0.0019	0.0042	0.0084	0.0055	0.0097	0.0016	0.0047

**Table 4-10:** Response Matrix Error ( $k = 4, n = 32$ ) ( $\times 10^{-5}$ )

0.0911	0.0254	0.0130	0.0121	0.0566	0.1247	0.1134	0.0731
0.0318	0.0214	0.0220	0.0094	0.0572	0.1300	0.1035	0.0640
0.0183	0.0276	0.0791	0.0194	0.0308	0.1345	0.1712	0.0956
0.0329	0.0141	0.0226	0.0215	0.0314	0.0622	0.0736	0.1118
0.0283	0.0117	0.0168	0.0514	0.0955	0.1109	0.1063	0.0579
0.0690	0.0412	0.0477	0.0510	0.0714	0.2107	0.0767	0.0201
0.0730	0.0270	0.0707	0.0284	0.0697	0.1654	0.0762	0.0885
0.0735	0.0248	0.0391	0.0412	0.0661	0.0886	0.1238	0.1174

**Table 4-11:** Response Matrix Error ( $k = 7, n = 16$ )

0.8698	0.4196	0.2543	0.2915	0.3348	0.2221	0.1374	0.2425
0.1707	0.1970	0.0767	0.3016	0.2849	0.2178	0.1841	0.2734
0.2203	0.1015	0.2467	0.2579	0.0581	0.1432	0.2819	0.1617
0.3603	0.2876	0.2826	0.5804	0.3007	0.1418	0.0931	0.2100
0.3004	0.3245	0.1513	0.0518	0.8034	0.3260	0.2449	0.2108
0.2814	0.3015	0.0607	0.0567	0.1797	0.7652	0.4636	0.2064
0.1767	0.1392	0.3385	0.2292	0.1358	0.5007	0.0239	0.4479
0.2623	0.1648	0.1438	0.3322	0.1642	0.1731	0.2737	0.2779

**Table 4-12:** Response Matrix Error ( $k = 7, n = 32$ )

0.0002	0.0000	0.0001	0.0004	0.0009	0.0013	0.0006	0.0004
0.0000	0.0001	0.0001	0.0000	0.0005	0.0007	0.0001	0.0001
0.0002	0.0001	0.0001	0.0000	0.0002	0.0006	0.0008	0.0003
0.0005	0.0000	0.0000	0.0000	0.0000	0.0002	0.0001	0.0008
0.0008	0.0006	0.0001	0.0001	0.0003	0.0003	0.0007	0.0009
0.0014	0.0007	0.0005	0.0002	0.0003	0.0003	0.0002	0.0004
0.0006	0.0002	0.0011	0.0002	0.0008	0.0003	0.0005	0.0005
0.0003	0.0002	0.0004	0.0008	0.0011	0.0003	0.0005	0.0003

**Figure 4-14** shows the result of the inverse problem for “Paw” shape using far field response matrix data. Again, the low frequency result is robust but not accurate. The high frequency result is accurate but not robust, with quite some numerical artifacts. The multiple frequency result is both accurate and robust.

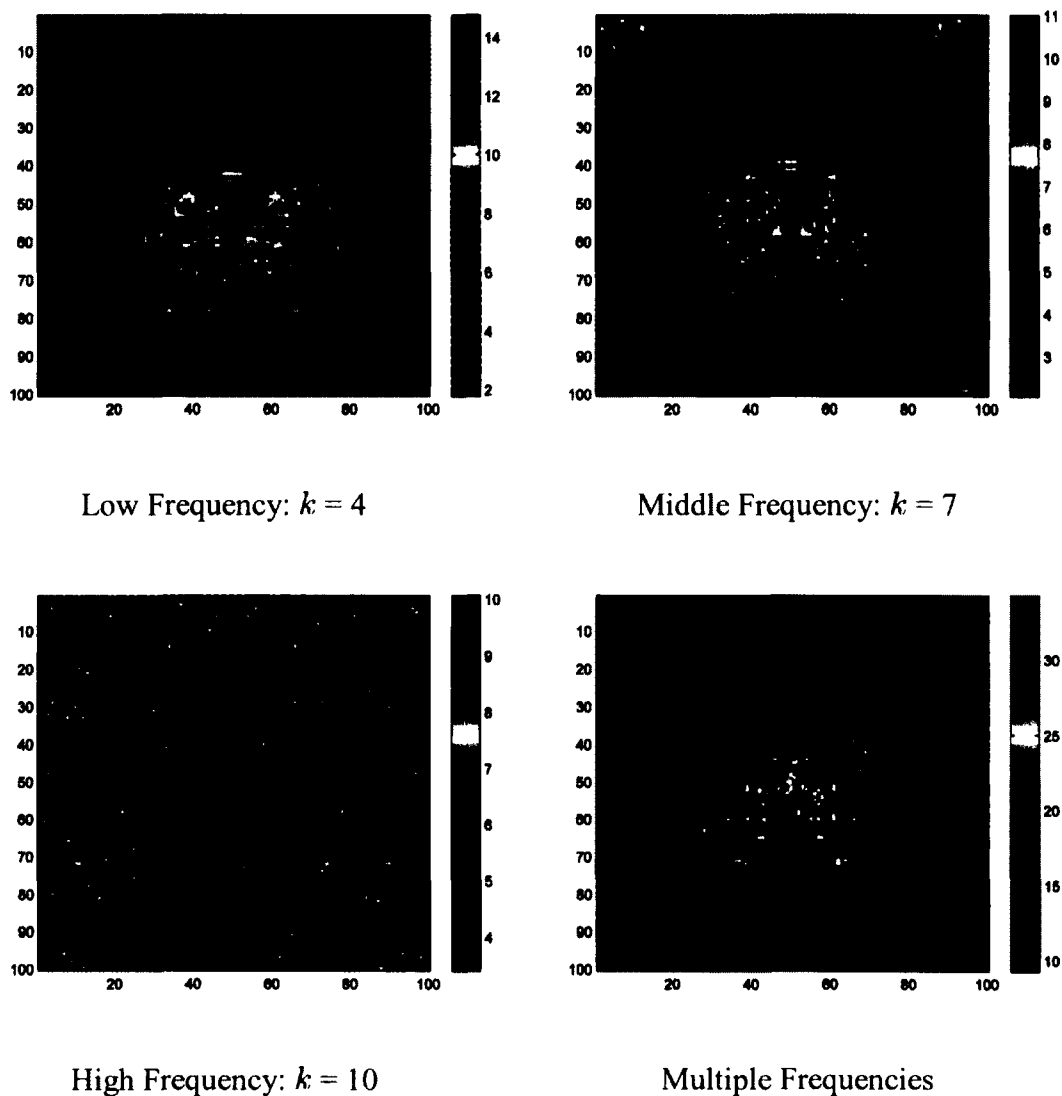


**Figure 4-14:** “Paw” with Plane Incident Wave, Far Field Data.

We next present an example with multiple targets. **Figure 4-15** shows the result using low frequency data. It allows us to localize the five shapes, but with no details. **Figure 4-16** shows the high frequency result with details, but less robustness. With the help from low frequency result, we would zoom the five regions one by one. For example, **Figure 4-17** shows the zoomed result for the butterfly shape in the middle using high frequency data.

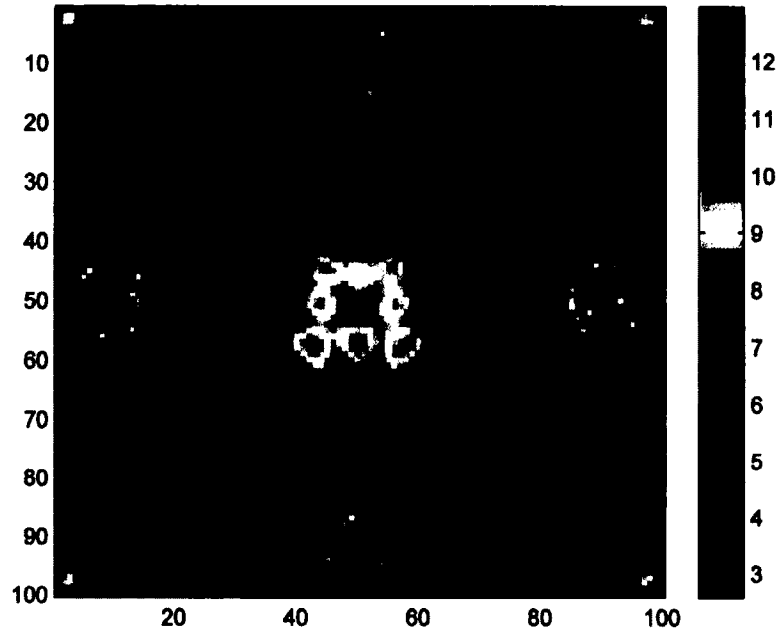


Figure 4-15: Low Frequency Result for Multiple Targets.

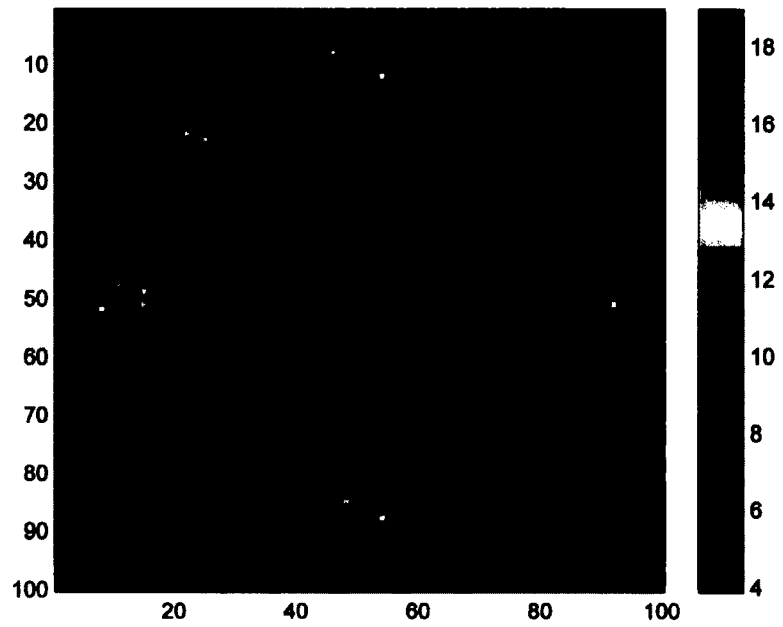
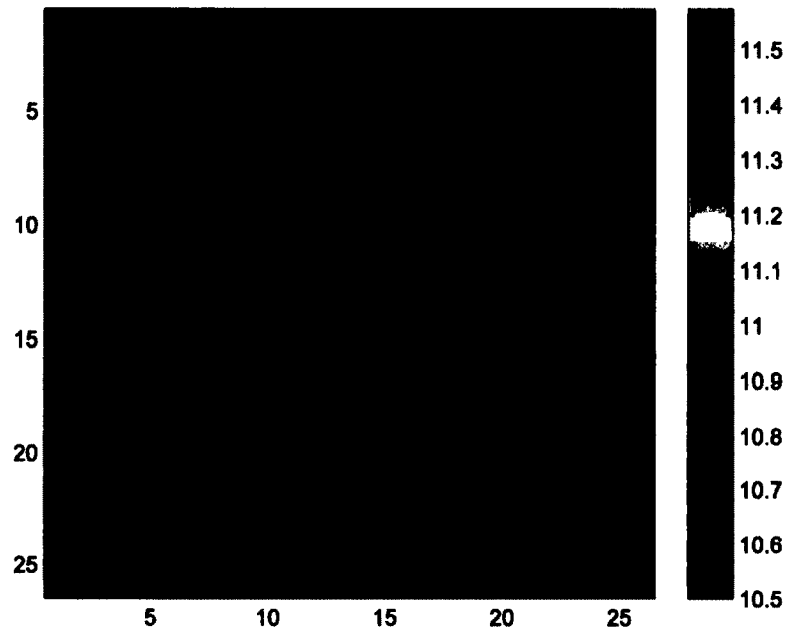


Figure 4-16: High Frequency Result for Multiple Targets.



**Figure 4-17:** Zooming the Butterfly Shape Part using High Frequency.

## **CHAPTER 5**

### **CONCLUSIONS AND FUTURE WORK**

#### **5.1 Conclusions**

We proposed numerical methods for solving the direct and inverse scattering problems for domains with multiple corners. For the forward problem, we extended the method in [1]. The resulting method is well-conditioned. Instead of exponential convergence for the smooth target case, high order convergence is observed for the case with multiple corners. For the inverse problem, we proposed a method similar to the MUSIC algorithm in [25] and [26], but we keep the phase information so that multiple frequency data can be combined. Numerical results showed that our method is efficient, accurate and robust. We also studied the response matrix relations for near and far field data, as well as singular value perturbation.

#### **5.2 Future Work**

There are several future directions we could work on. First, we could consider the Neumann problem instead of the Dirichlet problem. Although the smooth target case for the Neumann problem has been solved with exponential convergence, the challenging problem with multiple corners remains open.

Second, we could consider the three dimensional direct and inverse scattering problems. The concept of signal space and noise space as well as illumination vectors can be generalized to three space dimensions. The MUSIC algorithm or multi-tone algorithm or other methods of such type could therefore be generalized to solve three-dimensional problems as well. A forward solver could also be developed for three-dimensional problems.

Third, we could work on the problem with random background medium by using the effective Green's function; [14] has some preliminary work in this area and our imaging algorithm could be modified using effective Green's function to replace homogeneous Green's function.

## BIBLIOGRAPHY

- [1] D. Colton and R. Kress, *Inverse acoustic and electromagnetic scattering theory*, 2nd ed., Appl. Math. Sci. 93, Springer-Verlag, Berlin (1998).
- [2] E. Martensen, *Über eine Methode zum räumlichen Neumannschen Problem mit einer Anwendung für torusartige Berandungen*, Acta Math, 109 (1963), pp. 75-135.
- [3] R. Kussmaul, *Ein numerisches Verfahren zur Lösung des Neumannschen Aussenraumproblems für die Helmholtzsche Schwingungsgleichung*, Computing 4 (1969), pp. 246-273.
- [4] D. Colton and P. Monk, *A novel method for solving the inverse scattering problem for time-harmonic acoustic waves in the resonance region*, SIAM J. Appl. Math., 45 (1985), pp.1039-1053.
- [5] D. Colton and P. Monk, *A novel method for solving the inverse scattering problem for time-harmonic acoustic waves in the resonance region II*, SIAM J. Appl. Math., 46 (1986), pp. 506-523.
- [6] Yves Nievergelt, *Schmidt-Mirsky matrix approximation with linearly constrained singular values*, Linear Algebra and its Applications. Vol. 261 (1997), pp. 207-219.
- [7] R. Potthast, *A fast new method to solve inverse scattering problems*, Inverse Problems, 12 (1996), pp. 731-742.

- [8] R. Potthast, *A point-source method for inverse acoustic and electromagnetic obstacle scattering problems*, IMA J. Appl. Math., 61 (1998), pp. 119-140.
- [9] R. Potthast, *Point sources and multipoles in inverse scattering theory*, Chapman and Hall, London (2001).
- [10] M. Ikehata, *Reconstruction of an obstacle from the scattering amplitude at a fixed frequency*, Inverse Problems, 14 (1998), pp. 949-954.
- [11] M. Ikehata, *Enclosing a polygonal cavity in a two-dimensional bounded domain from Cauchy data*, Inverse Problems, 15 (1999), pp. 1231-1241.
- [12] M. Ikehata, *On reconstruction in the inverse conductivity problem with one measurement*, Inverse Problems, 16 (2000), pp. 785-793.
- [13] G. Stewart and G. Sun, *Matrix perturbation theory*, Computer Science and Scientific Computing Academic Press, Inc., Boston, MA, 1990.
- [14] S. Luo, J. Qian and R. Burridge, *Fast Huygens sweeping methods for Helmholtz equations in inhomogeneous media in the high frequency regime*, Journal of Comput. Physics, 270 (2014), pp. 378-401.
- [15] G. Bao and P. Li, *Inverse medium scattering for the Helmholtz equation at fixed frequency*, Inverse Problems, 21 (2005), pp. 1621-1641.
- [16] G. Bao and P. Li, *Numerical solution of inverse scattering for near-field optics*, Optics Letters, 32 (11) (2007), pp. 1465-1467.
- [17] Y. Chen, *Inverse scattering via Heisenberg uncertainty principle*, Inverse Problems, 13 (1997), pp. 253-282.
- [18] Y. Chen, *Inverse scattering via skin effect*, Inverse Problems, 13 (1997), pp. 649-667.

- [19] G. Bao and P. Li, *Inverse medium scattering for three-dimensional time harmonic Maxwell equations*, *Inverse Problems*, 20 (2004), pp. L1-L7.
- [20] G. Bao, P. Li, *Inverse medium scattering problems for electromagnetic waves*, *SIAM J. Appl. Math.*, 65 (2005), pp. 1006-2049.
- [21] G. Stewart, *Stochastic perturbation theory*, *SIAM Rev.* 32, Vol. 4 (1990), pp. 579-620.
- [22] S. Hou, K. Solna and H. Zhao, *Imaging of location and geometry for extended targets using the response matrix*, *J. Comp. Phys.*, Vol. 199 (2004), pp. 317-338.
- [23] O. Panic, *On the question of the solvability of the exterior boundary-value problems for the wave equation and Maxwell's equations*, *Usp. Mat. Nauk*, 20A (1965), pp. 221-226.
- [24] D. Colton, J. Coyle and P. Monk, *Recent developments in inverse acoustic scattering theory*, *SIREV*, 42 (2000), pp. 369-414.
- [25] S. Hou, K. Solna, and H. Zhao, *A direct imaging algorithm for extended targets*, *Inverse Problems*, 22 (2006), pp. 1151-1178.
- [26] S. Hou, K. Solna, and H. Zhao, *A direct imaging method for far field data*, *Inverse Problems*, 23 (2007), pp. 1533-1546.
- [27] S. Hou, K. Huang, K. Solna, and H. Zhao, *A phase and space coherent direct imaging algorithm*, *J. Acoust. Soc. Am*, 125 (2009), pp. 227-238.
- [28] A. Kirsch, *Characterization of the shape of a scattering obstacle using the spectral data of the far-field operator*, *Inverse Problems*, 14 (1998), pp. 1489-1512.

- [29] G. Bao, S. Hou and P. Li, *Imaging scattering by a continuation method with initial guesses from a direct imaging algorithm*, J. Comp. Phys., Vol. 227 (2007), pp. 755–762.
- [30] C. Li and R. Mathias, *The Lidskii-Mirsky-Wielandt theorem – additive and multiplicative versions*, Numer. Math., 81 (1999), pp. 377-413.
- [31] G. Bao and P. Li, *Inverse medium scattering problems for electromagnetic waves*, SIAM J. Appl. Math., 65 (2005), pp. 2049-1066.
- [32] G. Bao and P. Li, *Inverse medium scattering for the Helmholtz equation at fixed frequency*, Inverse Problems, 21 (2005), pp. 1621-1641.
- [33] G. Bao and P. Li, *Numerical solution of inverse scattering for near-field optics*, Optics Letters, Vol. 32 (2007), pp. 1465-1467.
- [34] Y. Chen, *Inverse scattering via Heisenberg uncertainty principle*, Inverse Problems, 13 (1997), pp. 253-282.
- [35] Y. Chen, *Inverse scattering via skin effect*, Inverse Problems, 13 (1997), pp. 649-667.
- [36] O. Dorn, E. Miller, and C. Rappaport, *A shape reconstruction method for electromagnetic tomography using adjoint fields and level sets*, Inverse Problems, 16 (2000), pp. 1119–1156.
- [37] L. Mirsky, *Symmetric gauge function and unitarily invariant norms*, Quart. J. Math., Vol. 11 (1960), pp. 50-59.
- [38] R. Schmidt, *Multiple emitter location and signal parameter estimation*, IEEE Trans. Antennas Propagation, 34(1986), pp.276-280.

- [39] J.P. Berenger, *A perfectly matched layer for the absorption of electromagnetic waves*, J. Comp. Phys., Vol. 114 (1994), pp. 185–200.
- [40] S. Tsynkov and E. Turkel, *A Cartesian perfectly matched layer for the Helmholtz equation*, Absorbing Boundaries and Layers, Domain Decomposition Methods, Nova Science Publishers, New York (2001), pp. 279–309.
- [41] H. Zhao, *Analysis of the response matrix for an extended target*, SIAM Applied Mathematics, Vol. 64 (2004), pp. 725-745.
- [42] D. Colton and A. Kirsch, *A simple method for solving inverse scattering problems in the resonance region*, Inverse Problems, 12 (1996), pp. 383-393.
- [43] S. Hou, Y. Jiang and Y. Cheng, *Direct and Inverse Scattering Problems for Domains with Multiple Corners*, International Journal of Partial Differential Equations, Vol. 2015, Article ID 968529 (2015).